



AFRL-RZ-WP-TP-2008-2230

THE EFFECT OF DISSOLVED AIR ON THE COOLING PERFORMANCE OF A PARTIALLY CONFINED FC-72 SPRAY

Rebekah L. Puterbaugh, Kirk L. Yerkes, and Scott K. Thomas

**Engine Integration and Assessment Branch
Turbine Engine Division**

**JULY 2008
Final Report**

Approved for public release; distribution unlimited.

See additional restrictions described on inside pages

**AIR FORCE RESEARCH LABORATORY
PROPULSION DIRECTORATE
WRIGHT-PATTERSON AIR FORCE BASE, OH 45433-7251
AIR FORCE MATERIEL COMMAND
UNITED STATES AIR FORCE**

NOTICE AND SIGNATURE PAGE

Using Government drawings, specifications, or other data included in this document for any purpose other than Government procurement does not in any way obligate the U.S. Government. The fact that the Government formulated or supplied the drawings, specifications, or other data does not license the holder or any other person or corporation; or convey any rights or permission to manufacture, use, or sell any patented invention that may relate to them.

This report was cleared for public release by the USAF 88th Air Base Wing (88 ABW) Public Affairs Office (PAO) and is available to the general public, including foreign nationals. Copies may be obtained from the Defense Technical Information Center (DTIC) (<http://www.dtic.mil>).

AFRL-RZ-WP-TP-2008-2230 HAS BEEN REVIEWED AND IS APPROVED FOR PUBLICATION IN ACCORDANCE WITH ASSIGNED DISTRIBUTION STATEMENT.

*//Signature//

REBEKAH L. PUTERBAUGH
Project Manager
Engine Integration and Assessment Branch
Turbine Engine Division

//Signature//

THOMAS REITZ, Branch Chief
Electrochemistry & Thermal Sciences Branch
Power Division
Propulsion Directorate

//Signature//

KIRK L. YERKES
Deputy for Science
Power Division
Propulsion Directorate

This report is published in the interest of scientific and technical information exchange and its publication does not constitute the Government's approval or disapproval of its ideas or findings.

*Disseminated copies will show “//Signature//” stamped or typed above the signature blocks.

REPORT DOCUMENTATION PAGE				Form Approved OMB No. 0704-0188	
<p>The public reporting burden for this collection of information is estimated to average 1 hour per response, including the time for reviewing instructions, searching existing data sources, gathering and maintaining the data needed, and completing and reviewing the collection of information. Send comments regarding this burden estimate or any other aspect of this collection of information, including suggestions for reducing this burden, to Department of Defense, Washington Headquarters Services, Directorate for Information Operations and Reports (0704-0188), 1215 Jefferson Davis Highway, Suite 1204, Arlington, VA 22202-4302. Respondents should be aware that notwithstanding any other provision of law, no person shall be subject to any penalty for failing to comply with a collection of information if it does not display a currently valid OMB control number. PLEASE DO NOT RETURN YOUR FORM TO THE ABOVE ADDRESS.</p>					
1. REPORT DATE (DD-MM-YY) July 2008		2. REPORT TYPE Final		3. DATES COVERED (From - To) 24 October 2005 – 16 June 2006	
4. TITLE AND SUBTITLE THE EFFECT OF DISSOLVED AIR ON THE COOLING PERFORMANCE OF A PARTIALLY CONFINED FC-72 SPRAY				5a. CONTRACT NUMBER In-house	
				5b. GRANT NUMBER	
				5c. PROGRAM ELEMENT NUMBER 62203F	
6. AUTHOR(S) Rebekah L. Puterbaugh (AFRL/RZTA) Kirk L. Yerkes (AFRL/RZPS) Scott K. Thomas (Wright State University)				5d. PROJECT NUMBER 3145	
				5e. TASK NUMBER 20	
				5f. WORK UNIT NUMBER 314520C9	
7. PERFORMING ORGANIZATION NAME(S) AND ADDRESS(ES) Engine Integration and Assessment Branch (AFRL/RZTA) Turbine Engine Division Electrochemistry & Thermal Sciences Branch (AFRL/RZPS) Power Division Air Force Research Laboratory, Propulsion Directorate Wright-Patterson Air Force Base, OH 45433-7251 Air Force Materiel Command, United States Air Force				8. PERFORMING ORGANIZATION REPORT NUMBER AFRL-RZ-WP-TP-2008-2230	
9. SPONSORING/MONITORING AGENCY NAME(S) AND ADDRESS(ES) Air Force Research Laboratory Propulsion Directorate Wright-Patterson Air Force Base, OH 45433-7251 Air Force Materiel Command United States Air Force				10. SPONSORING/MONITORING AGENCY ACRONYM(S) AFRL/RZTA	
				11. SPONSORING/MONITORING AGENCY REPORT NUMBER(S) AFRL-RZ-WP-TP-2008-2230	
12. DISTRIBUTION/AVAILABILITY STATEMENT Approved for public release; distribution unlimited.					
13. SUPPLEMENTARY NOTES PAO Case Number: 88ABW-2008-0138; Clearance Date: 11 Sep 2008. This report is a thesis.					
14. ABSTRACT The objective of this thesis is to investigate the heat transfer performance of a partially confined FC-72 spray with varying dissolved air concentrations. An experimental test rig consisting of a spray chamber coupled to a fluid delivery loop system was used to obtain temperature, pressure, and critical heat flux (CHF) data. A downward facing nozzle within the spray chamber allowed the FC-72 fluid to be sprayed onto an upward facing, thick-film, resistor heater. The heater was mounted onto a glass post, with a sump system to allow removal of excess fluid. Type-E thermocouples were imbedded in the post to obtain temperature data. The parametric ranges for experimental testing were as follows: volume-percent concentration of dissolved air, $5 \leq C_m \leq 18\%$, chamber pressure, $6.90 \times 10^4 \leq P_{ch} \leq 8.27 \times 10^4 \text{ N/m}^2$ ($10 \leq P_{ch} \leq 12 \text{ psia}$), subcooling, $2 \leq \Delta T_{sc} \leq 12^\circ\text{C}$, volumetric flow rate, $6.31 \leq \dot{V} \leq 10.5 \text{ cm}^3/\text{s}$ ($6.0 \leq \dot{V} \leq 10.0 \text{ gph}$). Test data were obtained for comparison of CHF with varying C while controlling the spray chamber pressure. No significant variation in heat transfer performance was observed. The applicability of Henry's law to the current system was investigated, and air concentration measurements using Henry's law were compared with those obtained using a direct sample method.					
15. SUBJECT TERMS spray cooling, dissolved air, FC-72					
16. SECURITY CLASSIFICATION OF:			17. LIMITATION OF ABSTRACT: SAR	18. NUMBER OF PAGES 112	19a. NAME OF RESPONSIBLE PERSON (Monitor) Rebekah L. Puterbaugh 19b. TELEPHONE NUMBER (Include Area Code) N/A
a. REPORT Unclassified	b. ABSTRACT Unclassified	c. THIS PAGE Unclassified			

TABLE OF CONTENTS

I. Introduction	1
II. Experimental Design and Test Procedure	13
III. Empirical Mathematical Relationship.....	23
IV. Results and Discussion	31
V. Conclusions.....	44
Appendix A: Procedures	47
Appendix B: Thermocouple Calibration.....	55
Appendix C: Error Analysis.....	57
References.....	95

LIST OF FIGURES

Figure 1: Heat transfer coefficients: various processes and coolants (Mudawar, 2001)	1
Figure 2: Boiling regimes as a function of heat flux and wall superheat	3
Figure 3: Representative F-15 flight profile (Yerkes and Beam, 1992)	6
Figure 4: Experimental test rig (Baysinger et al., 2004).....	13
Figure 5: Experimental test chamber (Yerkes et al., 2006)	14
Figure 6: Pedestal and sump arrangement (Yerkes et al., 2006)	15
Figure 7: Flow loop schematic for the experimental test rig	16
Figure 8: Heater pedestal side view (Yerkes et al., 2006)	17
Figure 9: Heater layer dimensions and thermal conductivities (not to scale).....	17
Figure 10: Heater pedestal components (Baysinger, 2005)	18
Figure 11: Fully assembled heater pedestal (Yerkes et al., 2006)	18
Figure 12: Heater pedestal top view with thermocouples (Yerkes et al., 2006).....	19
Figure 13: Membrane filter used for removal of air from FC-72	20
Figure 14: Variation in C_m with P_{ch}	20
Figure 15: Aire-ometer used for measuring dissolved gas concentration in fluids	21
Figure 16: Thick film resistor heater schematic (not to scale).....	23
Figure 17: Cover geometry with boundary conditions	24
Figure 18: Heater geometry with boundary conditions	25
Figure 19: Substrate geometry with boundary conditions	26
Figure 20: q vs ΔT showing key points for coefficient determination.....	27
Figure 21: Functional relationship equations for $q_{(\Delta T=0)}$; $C_m = 10\%$, $10 \leq \Delta T_{sc} \leq 12^\circ\text{C}$, and $\dot{V} = 6.31, 8.41, \text{ and } 10.5 \text{ cm}^3/\text{s}$	28
Figure 22: Functional relationship equations for q_{CHF} ; $C_m = 10\%$, $10 \leq \Delta T_{sc} \leq 12^\circ\text{C}$, and $\dot{V} = 6.31, 8.41, \text{ and } 10.5 \text{ cm}^3/\text{s}$	29

Figure 23: Functional relationship equations for ΔT_{CHF} ; $C_m = 10\%$, $10 \leq \Delta T_{sc} \leq 12^\circ\text{C}$, and $\dot{V} = 6.31, 8.41$, and $10.5 \text{ cm}^3/\text{s}$	29
Figure 24: Heater temperature variation with time	34
Figure 25: q versus ΔT for Set 1	36
Figure 26: q versus ΔT for Set 2	36
Figure 27: q versus ΔT for Set 3	37
Figure 28: q versus ΔT for Set 4	37
Figure 29: Critical heat flux (CHF) with varying air content for volume-percent	39
Figure 30: Mathematical fit with experimental data included	43
Figure 31: Sample thermocouple calibration plot	56

LIST OF TABLES

Table 1: Experimental results including precision error only.....	35
Table 2: Molar ratio comparison including precision error only.....	42
Table 3: Research parameters and results.....	45
Table 4: Research parameters and results (continued).	46
Table 5: FC-72 Volumetric flow rate, with error.....	73
Table 6: Subcooled temperature, with error	74
Table 7: Saturation temperature corresponding to chamber pressure, with error.....	75
Table 8: Interface and surface heater temperatures, with error	76
Table 9: Average chamber pressure, with error.....	77
Table 10: Critical heat flux and heater power, with error.....	78
Table 11: Heater and resistor voltages and resistance, with error	79
Table 12: Measured air content by volume and measured air volume ratio, with error	80
Table 13: Corrected air volume ratio and corrected air content by volume, with error	81
Table 14: Measured molar ratio from measured air volume ratio, with error	82
Table 15: Molar ratio from corrected air volume ratio, with error	83
Table 16: Reference total pressure, with error.....	84
Table 17: Reference saturation pressure, with error	85
Table 18: Reference chamber temperature, with error	86
Table 19: Reference partial pressure, with error.....	87
Table 20: Reference FC-72 and air densities, with error	88
Table 21: Molar ratios calculated using Henry's law, with error	89
Table 22: Total pressure, with error.....	90
Table 23: Saturation pressure, with error.....	91
Table 24: Chamber temperature, with error.....	92
Table 25: Partial Pressure, with error	93
Table 26: FC-72 and air densities, with error	94

ABSTRACT

Puterbaugh, Rebekah Lee. M.S.E., Department of Mechanical and Materials Engineering, Wright State University, 2008. The Effect of Dissolved Air on the Cooling Performance of a Partially Confined FC-72 Spray.

The objective of this thesis is to investigate the heat transfer performance of a partially-confined FC-72 spray with varying dissolved air concentrations. An experimental test rig consisting of a spray chamber coupled to a fluid delivery loop system was used to obtain temperature, pressure, and critical heat flux (CHF) data. A downward facing nozzle within the spray chamber allowed the FC-72 fluid to be sprayed onto an upward facing, thick-film, resistor heater. The heater was mounted onto a glass post, with a sump system to allow removal of excess fluid. Type-E thermocouples were imbedded in the post to obtain temperature data. The parametric ranges for experimental testing were as follows: volume-percent concentration of dissolved air, $5 \leq C_m \leq 18\%$, chamber pressure, $6.90 \times 10^4 \leq P_{ch} \leq 8.27 \times 10^4 \text{ N/m}^2$ ($10 \leq P_{ch} \leq 12 \text{ psia}$), subcooling, $2 \leq \Delta T_{sc} \leq 12^\circ\text{C}$, volumetric flow rate, $6.31 \leq \dot{V} \leq 10.5 \text{ cm}^3/\text{s}$ ($6.0 \leq \dot{V} \leq 10.0 \text{ gph}$). Test data were obtained for comparison of CHF with varying C while controlling the spray chamber pressure. No significant variation in heat transfer performance was observed. The applicability of Henry's law to the current system was investigated, and air concentration measurements using Henry's law were compared with those obtained using a direct sample method. The resulting air concentration measurements did not agree. An empirical mathematical relationship allowing for determination of surface heat flux with varying flow rate was also developed. The relationship was obtained using test data at flow rates of $\dot{V} = 6.31, 8.41, \text{ and } 10.5 \text{ cm}^3/\text{s}$ ($6.0, 8.0, \text{ and } 10.0 \text{ gph}$), and was validated using experimental data obtained for flow rates of $\dot{V} = 7.36 \text{ and } 9.46 \text{ cm}^3/\text{s}$ ($7.0 \text{ and } 9.0 \text{ gph}$).

NOMENCLATURE

a	acceleration level, g
C	% air content by volume, $[V_{\text{air}} / (V_{\text{FC}} + V_{\text{air}})] \times 100$
C^*	air volume ratio, $(V_{\text{air}} / V_{\text{FC}})$
D_p	droplet diameter, m
f	heater conduction loss fraction
f^*	function, for error calculation
Fr	Froude number, v^2/aD_p
Ga	Galileo number, $aD_p^3\rho^2/\mu^2$
H	Henry's constant, mol/mol-kPa
h	heat transfer coefficient, $W/(m^2\cdot K)$
k	thermal conductivity, $W/(m\cdot K)$
M	molar fraction, $N_{\text{air}} / (N_{\text{FC}} + N_{\text{air}})$
M^*	molar ratio, $(N_{\text{air}} / N_{\text{FC}})$
m	molar mass, g/mol
N	number of moles
P	pressure, N/m^2
P_g	partial pressure, N/m^2
q	heat flux, W/m^2
Q	heat load, W
R	resistance, Ω
t	time, s
T	temperature, K
v	velocity, m/s
\dot{V}	volumetric flow rate, m^3/s
V	voltage, V
V	volume, m^3

We	Weber Number, $\rho v^2 D_p / \sigma$
Z	thickness, m
z	distance from bottom surface of heater conductive layer, m

Greek Letters

ρ	density, kg/m ³
μ	absolute viscosity, kg/m-s
σ	surface tension, kg/s ²
ΔT	$T_s - T_{\text{sat}}$, K
ΔT_{sc}	$T_f - T_{\text{sat}}$, fluid subcooling, K

Subscripts

air	air
amb	ambient
b	bottom of the heater conductive layer
ch	chamber
CHF	critical heat flux
cov	heater glass cover plate
FC	FC-72 fluid
htr	heater conductive layer
int	interface between heater substrate and insulating support post
m	measured
min	minimum
max	maximum
ref	reference value corresponding to rig conditions at time of fluid sample
s	heater surface
sat	saturation
sub	heater ceramic substrate
t	top of the heater conductive layer
tot	total
∞	freestream value

I. Introduction

As power capabilities increase with advancing technology, greater amounts of waste heat are being generated along with greater power. In addition, the power generating devices are being packaged in smaller spaces, causing increasingly large heat fluxes. Such heat fluxes must be managed as effectively and efficiently as possible. Since it takes advantage of the latent heat of vaporization, two-phase cooling is an area of heat transfer that can be extremely effective for high heat fluxes. Figure 1 shows the difference in heat transfer coefficients that can be obtained when using two-phase cooling as opposed to single-phase cooling.

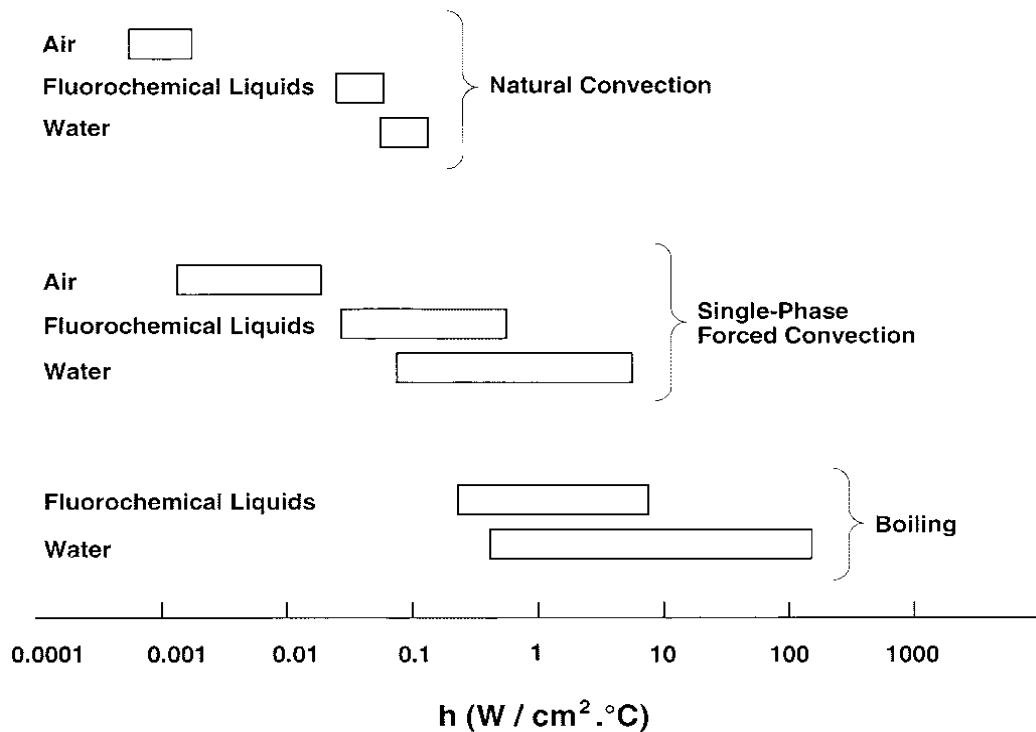


Figure 1. Heat transfer coefficients: various processes and coolants (Mudawar, 2001).

In two-phase cooling a phase change of liquid to vapor, or boiling, occurs. The boiling process has varying regimes which occur as heat is transferred from a solid surface to a liquid in contact with that surface. Included in the regimes are free convection, nucleate boiling, transition boiling, and film boiling. The boiling regimes are described well by Incropera and DeWitt (2002). Free convection is the first stage of boiling. The liquid in contact with the solid surface is heated and fluid motion is determined by temperature differences within the fluid itself. Bubble formation does not occur during free convection. In the nucleate boiling regime, bubbles of vapor begin to form at nucleation sites on the heated surface. The bubbles eventually release from the solid, allowing lower temperature fluid to come into contact with the hot surface. As the rate of heat transfer increases, nucleation sites become so abundant that the fluid moves into transition boiling, and eventually film boiling. During transition boiling, the fluid at the hot surface oscillates between boiling at nucleation sites and developing a film of vapor on the heated surface. Once the oscillation stops, film boiling takes over, and the heated surface is completely covered by a thin vapor layer. Heat transfer to the fluid is drastically reduced during transition and film boiling due to the inability of the cooler fluid to reach the heated surface. The primary heat transfer modes become conduction and radiation, as opposed to convection to the cooler fluid.

Figure 2 shows a typical boiling curve for cooling liquids. The onset of nucleate boiling, or the point at which bubbles start forming on the solid surface, is shown. Critical heat flux (CHF), the point at which maximum heat transfer is occurring, is also depicted, along with the Leidenfrost point, where minimum heat transfer is occurring. The solid line in the figure depicts the typical boiling curve that will be followed if the surface temperature of the substance being cooled is controlled. If the heat flux is controlled, however, the line depicted by arrows will be followed as the heat flux of the device is increased. Upon reaching critical heat flux, a sharp departure of the boiling curve will occur and the wall superheat will increase dramatically in a very short period of time.

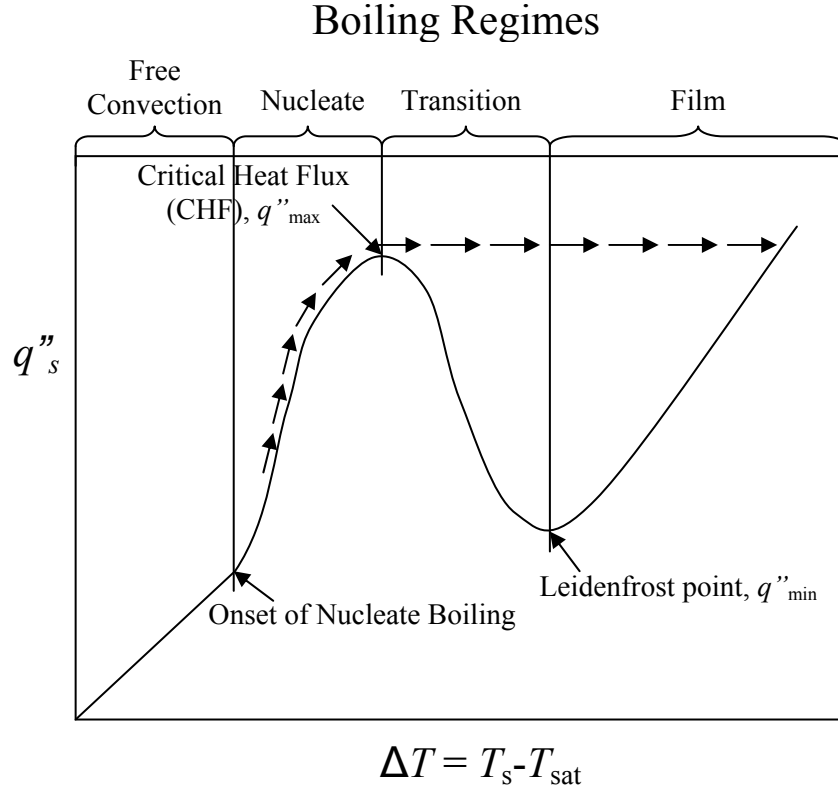


Figure 2. Boiling regimes as a function of heat flux and wall superheat.

Effective heat transfer occurs in the nucleate boiling regime during two-phase cooling. While free convection does facilitate some heat transfer, the nucleate boiling regime does so in markedly greater quantities. As can be seen in Fig. 2, the heat flux continues to increase dramatically after the onset of nucleate boiling until CHF is reached. If the wall superheat of the device is being controlled, after reaching CHF, the heat flux decreases dramatically and does not increase again until after the Leidenfrost point is reached. At the Leidenfrost point, droplets of fluid hover over their own vapor and do not actually come into contact with the heated surface. Because heat transfer through the vapor is low, the droplet evaporation time increases. After reaching the Leidenfrost point, heat transfer begins to increase again once film boiling is achieved as a result of radiation.

From the plot, it could be inferred that the optimal operating range for maximum heat transfer is at or near CHF. However, if CHF is exceeded, the surface temperature of the device being cooled could radically increase, jumping across the boiling curve

instantaneously. In power electronics, tight windows exist for the operating temperature. A sudden temperature spike could cause burnout of the device, making it unusable. As a result, operating parameters for any two-phase cooling system for application to power electronics must be fully investigated. An optimal cooling window must be defined so that maximum heat transfer will take place without the risk of damage to the device as a result of reaching CHF.

Several types of two-phase cooling methods exist. Pool boiling is utilized in devices such as thermosyphons to provide passive cooling. In this method, a pool of fluid is placed over the heat source. Heat is transferred from the solid surface to the liquid in contact with that surface. The heat is conducted through the liquid, forming thermal and density gradients, and causing fluid movement and free convection. As heat produced by the device increases, the fluid at the heated surface begins to boil and changes phase from liquid to vapor. As vapor bubbles form on the solid surface and are released, natural buoyancy carries them to the surface of the liquid, where the vapor is able to condense and falls back into the pool of liquid. This method is advantageous in many applications because of its passive nature, but is not always the most optimal cooling method.

Two-phase forced convection improves upon pool boiling because working fluid is forced over the hot surface. The forced flow generally has greater velocity than the free convection flow associated with pool boiling, and thus is associated with higher heat transfer coefficients. Although forced convection is not a passive cooling technique, the increased heat transfer coefficients make it an optimal choice in some cooling situations. Flow boiling is a type of two-phase forced convection that involves flow of the cooling fluid through a confined space, such as a channel, and can be employed in many different ways. In some instances, cooling fluid flows past the heat producing devices positioned in the channel. At other times, the channel walls themselves are the heated surface. In all instances, however, heat transfer occurs from the heated surface to the cooling fluid, forming vapor bubbles on the surface. Such bubbles are swept away by the forced flow of the cooling fluid through the channel. As the fluid sweeps past the heated surfaces, fresh fluid comes into contact with the heated surface, allowing continued heat transfer. Many parameters affect flow boiling, such as the size and geometry (Yang et al., 2008) of

the channels, along with the orientation of the channels (Zhang et al., 2005). The amount of heat transfer possible in flow boiling is also affected by the velocity of the flow and the amount of subcooling of the fluid (Mudawar and Maddox, 1989). One highly effective form of flow boiling is subcooled nucleate boiling, which is used in high heat flux applications. In this method, a liquid is forced over a heated surface, causing the liquid in contact with the surface to boil, while the bulk temperature of the fluid remains below the saturation temperature. It is one of the most efficient techniques for extremely high heat flux removal (Celata et al., 1993).

Jet impingement cooling involves the impact of a high velocity single-phase stream of fluid onto a surface. Fresh fluid is continuously supplied to the heated surface, while fluid which has already been used for heat transfer is pushed outward from the jet impact area. Some parameters that affect the heat transfer include jet diameter, velocity, and inlet subcooling (Yang et al., 2001). In two-phase jet impingement, the fluid boils as it impinges onto the heated surface, causing high heat transfer coefficients. While jet impingement is extremely effective, the large impact momentum on the heated surface can be damaging to delicate electronic equipment, making it an unsuitable cooling method for certain applications (Mudawar, 2001). Because the jet is concentrated in a single stream, the heat transfer is also concentrated, and notable temperature gradients can develop in the heated surface as a result. Such temperature gradients may also make jet impingement unsuitable for certain applications where a more constant temperature is needed throughout the device.

Spray cooling is similar to jet impingement; however, the liquid is broken up into very small droplets, which impact the heated surface separately. As a result, less impact momentum is associated with spray cooling than with jet impingement, making it a better cooling technique for delicate electronic equipment. Because the liquid impacts the surface in droplets instead of a single stream, the heat transfer is more uniform, creating a more constant temperature across the device, as opposed to the large temperature gradients associated with jet impingement (Estes and Mudawar, 1995). A comparison of the two methods in the non-boiling regime showed spray cooling was able to provide the same heat transfer coefficient as jet impingement with a substantially lower mass flux (Oliphant et al., 1998). The heat transfer obtained through the use of spray cooling is

very sensitive to flow rate and droplet size, along with nozzle geometry (Kim, 2007). As a result, the system must be well-characterized before being used in an application.

Because it encourages high heat transfer, and is gentle enough to be used with delicate equipment, spray cooling has been seen to have great potential in the area of power electronics cooling. One environment in which power electronics are used heavily is in application to aircraft. Before spray cooling can be employed in a system for that purpose, however, the performance limitations in such an environment must be properly addressed and defined. Aircraft inherently operate in conditions notably different than those experienced in terrestrial systems. Not the least of these differences involves variation in gravity. As a fighter jet goes through maneuvers, the gravity experienced on the aircraft can range anywhere from $-0.5 \leq a \leq 7\text{-g}$, as can be seen in Fig. 3.

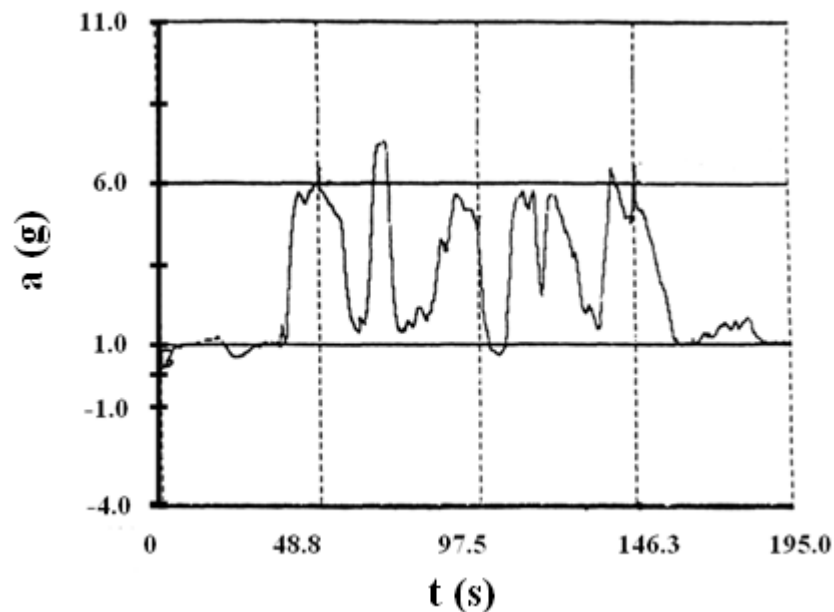


Figure 3. Representative F-15 flight profile (Yerkes and Beam, 1992).

Before a spray cooling system can be applied to power electronics cooling on such an aircraft, the spray must be adequately characterized in variable gravity.

A system was designed by Baysinger et al. (2004) to attempt to characterize a spray in variable gravity. A spray chamber was designed which included spray nozzles, heaters, and sumps to collect excess and condensed fluid. A fluid delivery and

management loop was connected to the spray chamber which included pumps, heat exchangers and a reservoir. Indium Tin Oxide (ITO) heaters attached to cylindrical polycarbonate pedestals were used as the heat source for the spray cooling experiments. To assist with the design, the entire system was modeled, and heat transfer analyses were performed for the spray chamber, fluid loops, and sumps. The system was flown on NASA's KC-135 reduced gravity research platform. Power was supplied to the ITO heater, but did not exceed $Q = 20 \text{ W}$, as the purpose of the flight was to evaluate the ability to maintain constant flow rate during testing in variable gravity. While the system was in reduced gravity, surface tension flow of unconstrained fluid was observed around the nozzle and sump. Variations in flow rate were observed throughout the flight, during both high and low gravity situations. Analytical calculations for transient temperature variation were performed and compared with experimental results. Good agreement was observed, particularly when a ramped heat input was used. It was estimated that 1% of the heat input was lost to the heater pedestal ($f \approx 1\%$). The spray heat transfer coefficient was estimated to be $h = 20,000 \text{ W/(m}^2\text{-K)}$ and the pedestal wall heat transfer coefficient was estimated to be $200 \leq h \leq 250 \text{ W/(m}^2\text{-K)}$.

Baysinger (2005) used the test rig to perform baseline spray cooling tests under terrestrial gravity conditions. Testing was performed on both a downward-facing nozzle spraying onto an upward-facing heater, and an upward-facing nozzle spraying onto a downward-facing heater. Subcooled FC-72 was used as the working fluid. Numerical analysis of the heat transfer throughout the heater pedestal was performed using finite element software. The numerical analysis, in combination with experimental data, allowed estimation of the heat transfer coefficient along the top of the heated surface. The heat transfer coefficient was estimated to range from $10,000 \leq h \leq 15,000 \text{ W/(m}^2\text{-K)}$ for $4.21 \leq \dot{V} \leq 10.52 \text{ cm}^3/\text{s}$ and $0 \leq Q \leq 50 \text{ W}$ for both the upward- and downward-facing heaters. The previous estimate for the amount of heat lost down the pedestal of $f \approx 1\%$ was adjusted to be $1.0 \leq f \leq 2.5\%$ as a result of analysis.

The test rig designed by Baysinger et al. (2004) was used in further experiments by Yerkes et al. (2006). The polycarbonate heater pedestals previously used were replaced with glass pedestals, and the heat transfer coefficients around the heater pedestal and conduction losses were determined using numerical and analytical analyses. The

numerical analysis was performed using a finite-element analysis. The pedestal was divided into two pieces, one being the ITO heater and the other being the glass post to which the heater was affixed. The ITO heater region was treated as a steady-state one-dimensional heat conduction problem with internal heat generation. The glass post was treated as a steady-state two-dimensional heat conduction problem, solving once for a semi-infinite rod solution, and once for a finite rod solution. The temperature at three locations in the heater pedestal was determined using both the numerical and analytical formulations. Thermocouples positioned at each of the three locations allowed comparison of the numerical, analytical and experimental results. The numerical and analytical formulations were also used to estimate the amount of heat lost down the heater pedestal. The test rig was flown again on NASA's reduced gravity platform. The Nusselt number was found to decrease with increasing $(Fr^{1/2}Ga)^{1/2}$ for a nominally fixed Weber number. The physical reason for such a result was not fully understood at the time, although possible explanations were given such as: variation in flow rate, recirculation of the spray film back onto the heater surface, influence of the partially-confined geometry over the heater surface, or effects of absorbed air in the FC-72 working fluid.

Upon observation of variable-gravity effects on the system, the possible effects of various other parameters on the cooling system were considered. One such parameter was determined to be dissolved air in the cooling fluid, as previously mentioned. It has been noted in previous research that the heat transfer associated with spray cooling is affected by the amount of dissolved air present in the cooling fluid. Although research has been conducted concerning this topic, the effect of dissolved air on spray cooling efficiency has not been completely characterized.

The effect of dissolved air on spray cooling with water as the working fluid was investigated by Milke et al. (1997). A solid plate of Macor, a glass-like material, was heated using radiant heaters, and spray cooled using a droplet dispenser positioned vertically over the tile. An infrared camera was used to record the transient thermal behavior of the Macor as the droplets were dispensed onto the surface and evaporated. Initial surface temperatures used in the experiment were $T_s = 110^\circ\text{C}$, 130°C , 150°C , 160°C , and 180°C . Air-saturated, deionized water was sprayed in a range of mass fluxes

from 0.24 to 1.6 g/(m²-s). Three varying mass fluxes were used for each initial temperature. The results from Milke's experiment were compared with results obtained in previous experiments involving degassed, deionized water, performed by Dawson and diMarzo (1993). For air-saturated water, as well as degassed water, the heated surface showed exponential cooling from the initial temperature to a steady state temperature. In the experiments involving air-saturated water, however, a lower steady state temperature was achieved than in those involving degassed water. To quantitatively compare the degassed and air-saturated results, the solid surface temperature drop along with a reference temperature was examined. The reference temperature was defined as the difference between the solid surface temperature at the onset of nucleate boiling for degassed water and the actual initial solid surface temperature. The ratio of the surface temperature change to the reference temperature was examined for air-saturated and degassed water spray cooling. For large ratios, the air-saturated and degassed water had similar cooling effects on the heated surface. For smaller ratios, however, it was observed that dissolved gases in the water enhanced cooling. The actual amount of dissolved air in the fluid was not calculated or measured.

The effect of dissolved air on spray cooling with FC-72 was addressed by Lin and Ponnappan (2003). A multi-nozzle plate containing eight miniature nozzles was used to spray cooling fluid over a surface area attached to a copper block heated by cartridge heaters. The nozzle array was used to investigate thermal performance data for various fluids, operating temperatures, nozzle pressure drops, and heat fluxes. To directly address the effect of dissolved air on the thermal performance of the system, tests were run using FC-72 as a working fluid. A test was run using liquid that had been degassed, and another was run using liquid containing a certain unspecified amount of air. The degassing method for the liquid was not mentioned, but a difference in chamber pressure verified the tests were run at differing air contents. The chamber pressure when using liquid containing air was $P_{ch} = 0.85$ bar while the pressure when using degassed fluid was $P_{ch} = 0.295$ bar. The volumetric flow rate per unit cooling area onto the heated surface was between $\dot{V} = 0.019$ and 0.0205 m³/(m²-s) for both tests. Results from the test involving degassed fluid indicated better thermal performance than that involving dissolved air up until CHF was reached. After reaching CHF, performance was better

when dissolved air was present. The surface temperature was higher when dissolved air was present for $q < 70 \text{ W/cm}^2$. For $q > 70 \text{ W/cm}^2$, however, the surface temperature was lower when dissolved air was present. The amount of dissolved gas was not directly measured or calculated.

Horacek et al. (2003) investigated the effect of dissolved air on spray cooling heat transfer using a full cone spray nozzle and microheater array. The test system was a closed flow loop including a spray chamber, condenser and pump. The array consisted of 96 microheaters maintained at a specified constant temperature using 96 separate Wheatstone bridge feedback circuits. The flow rate through the spray nozzle was set at $\dot{V} = 37 \text{ ml/min}$ ($0.62 \text{ cm}^3/\text{s}$). Saturation temperatures varied for each test, but were between $25^\circ\text{C} \leq T_{\text{sat}} \leq 65^\circ\text{C}$. FC-72 was used as a test fluid, and the amount of dissolved air in the fluid was controlled by varying the pressure within the test section using a vacuum pump. Five test cases were conducted with varying air content and thermal subcooling in the working fluid. As the amount of dissolved air in the working fluid was increased, the overall spray cooling efficiency was seen to increase when the five cases were compared. Heat flux was plotted as a function of wall temperature. On the plot, the cooling curves were shifted to the right as air content increased. CHF levels ranged from approximately $40 \leq q_{\text{CHF}} \leq 65 \text{ W/cm}^2$, increasing as the amount of air increased. The shift of the curves to higher temperatures as air content increased was attributed to higher saturation temperatures. Other reasons for the effect of the dissolved air were proposed, such as possible additional single phase convection of the heater areas not covered by drops. It was also theorized that the air may cause bubble nucleation within the spray droplets, increasing the liquid-solid contact area, or the liquid-vapor contact area. For the experiment, Henry's law was used to calculate the amount of dissolved air via partial pressure. Henry's law states that the solubility of a gas in a liquid at a given temperature is directly proportional to the partial pressure of the gas over the solution. For example, when the pressure exerted on a closed container with liquid and air inside is increased, the solubility of the air in the liquid is increased. Thus the liquid in the container is forced to absorb more air. While Henry's law provides a means of measuring the amount of dissolved air in the fluid, it does not provide a way of determining the distribution of the air in the flow loop.

Further work was done by Horacek et al. (2004) to investigate the effect of dissolved air on spray cooling heat transfer using measurements of time- and space-resolved heat transfer distributions and measurements of the liquid-solid contact area and three-phase contact line length. The experimental setup was similar to the previous experiment described above, with the same flow loop and heaters. A high-speed digital camera was used to record spray visualizations through the semi-transparent heater array. From the spray visualizations, areas of liquid-solid contact were measured using a total internal reflectance technique. The technique was implemented using a right angle prism in contact with the underside of the heater array. A light source was placed such that total internal reflection of the light occurred at the interface between the vapor in the chamber and the surface of the heater array. In the images taken by the camera, areas where vapor was in contact with the heater array surface would be bright while areas where liquid was in contact with the surface would form a dark region. As a result, the amount of area covered by liquid on the heater, along with the length of the three-phase contact line could be determined from the images. FC-72 was used as a cooling fluid.

The flow rate through the spray nozzle was set at $\dot{V} = 32 \text{ ml/min}$ ($0.62 \text{ cm}^3/\text{s}$). Five test cases were run. Thermal subcooling, or the temperature difference between the reservoir temperature and the liquid spray temperature, ranged from $-1.5 \text{ }^\circ\text{C}$ to $21.1 \text{ }^\circ\text{C}$ for the five tests. Gas subcooling, or the difference between the saturation temperature and the reservoir temperature, ranged from $3.6 \text{ }^\circ\text{C}$ to $39.6 \text{ }^\circ\text{C}$. As with the previous experiment, the overall spray cooling efficiency was seen to increase with increasing air content when the five cases were compared. CHF levels ranged from approximately $50 \leq q_{\text{CHF}} \leq 95 \text{ W/cm}^2$, increasing as the amount of dissolved air increased. The results from the experiment indicated that an increase in dissolved air within the fluid caused the saturation temperature of the fluid to increase, thereby increasing the subcooling of the fluid. The increase in subcooling then caused an increase in heat transfer. Visualization of the spray indicated that increased air content in the fluid caused intermittent dry regions to appear on the heater in greater number and frequency than in cases when air was not present. A proposed reason for this was the mass transport of the absorbed air escaping the liquid as it was heated. As in the previous work, partial pressures were used to calculate the amount of dissolved air in the liquid.

The objective of the present investigation was to determine the effect of absorbed air on critical heat flux with FC-72 as the working fluid while controlling the spray chamber pressure. For the current experiment, 3M Fluorinert FC-72 was chosen as the working fluid. The choice to use such a fluid was based on several reasons. FC-72 is dielectric, and thus can be sprayed directly onto electronic components, in this case, the thick film resistor heater, without causing damage due to electrical conduction. The saturation temperature and pressure of FC-72 is low enough that even when the fluid was boiling, everything on the test rig was still cool enough to touch. In addition, FC-72 is non-corrosive, non-toxic, non-flammable, and inert. Because the test rig was also used in variable gravity on NASA's reduced gravity aircraft, safety was a major concern, and inert fluid was required. In contrast to previous research, the amount of dissolved air per unit volume was measured directly. Because amounts of air as large as 48% by volume can be dissolved in FC-72 (3M, 1999), an understanding of the effect of dissolved air on surface heat flux is critical to understanding the general effectiveness of spray cooling using FC-72. For the experiment, data was collected over a range of volume-percent air content of approximately $5 \leq C_m \leq 18\%$, chamber pressure, $6.90 \times 10^4 \leq P_{ch} \leq 8.27 \times 10^4$ N/m² ($10 \leq P_{ch} \leq 12$ psia), and amount of subcooling, $2 \leq \Delta T_{sc} \leq 12^\circ\text{C}$. Each data set contained test runs at flow rates of $\dot{V} = 6.31, 8.41, \text{ and } 10.5 \text{ cm}^3/\text{s}$ (6.0, 8.0, and 10.0 gph), a specified air content by volume, C_m , chamber pressure, P_{ch} , and fluid subcooling, ΔT_{sc} . The percentage air by volume in the FC-72 was measured directly using an airmeter and fluid samples from the test rig, then corrected for experimental conditions using a ratio of partial pressures. An empirical mathematical model was also developed, relating surface heat flux to volumetric flow rate, subcooling, sensible heat, and CHF. The applicability of Henry's law and the use of partial pressures to calculate air concentration was considered and compared with the volume measurements.

II. Experimental Design and Test Procedure

The test rig used for experimentation was very similar to that described by Baysinger et al. (2004, 2005), and Baysinger (2005). There were, however, a few main differences. In the current experiment, glass pedestals replaced the polycarbonate pedestals described previously. The stainless steel reservoir in the FC-72 loop was replaced with an acrylic reservoir to allow visualization of the test fluid. Aluminum sumps replaced the polycarbonate sumps used in the initial rig design. The Indium Tin Oxide heater used previously was replaced with a thick film resistor heater.

A spray chamber coupled to a fluid delivery loop system made up the two main components of the test rig. A view of the entire test rig can be seen in Fig. 4, while a close-up of the chamber can be seen in Fig. 5.

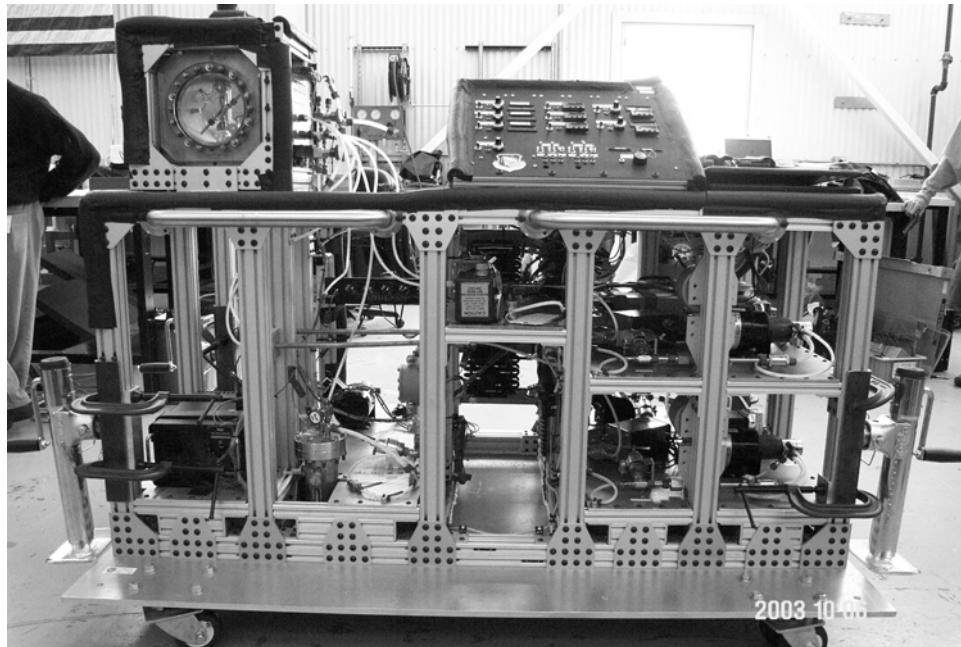


Figure 4. Experimental test rig (Baysinger et al., 2004).

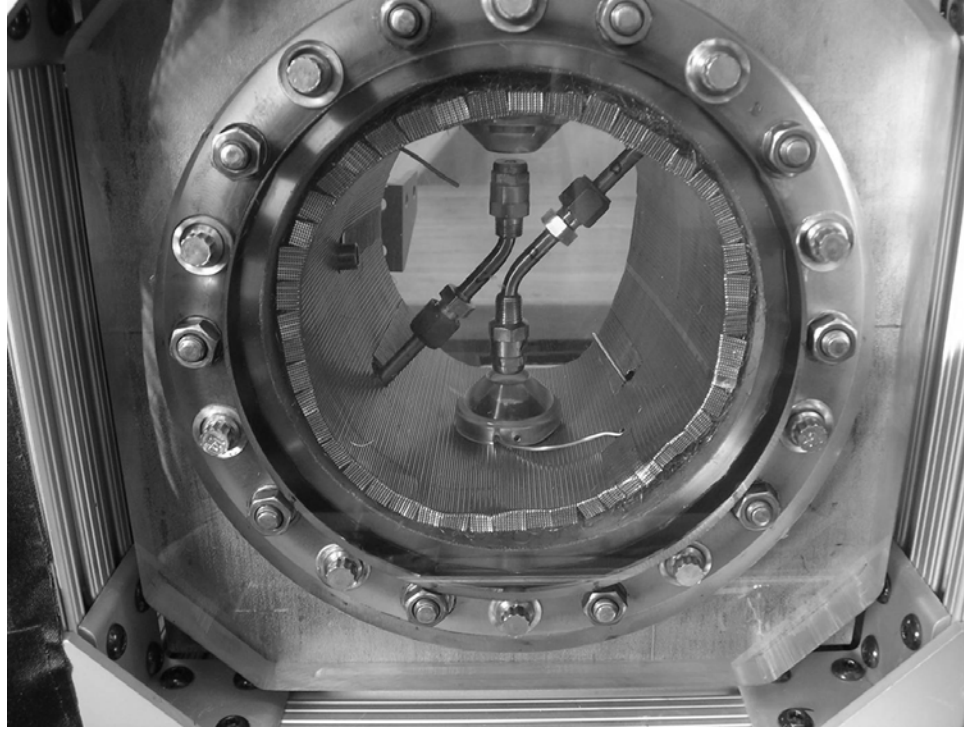


Figure 5. Experimental test chamber (Yerkes et al., 2006).

The structural frame of the test rig was composed of T-slotted aluminum extrusions. The spray chamber was cylindrical, with a cooling jacket surrounding the circular frame. The end caps were fabricated of thick acrylic plates to allow visualization during experimentation. Within the spray chamber, two opposing nozzles allowed fluid to be sprayed onto two opposing thick-film resistor heaters manufactured by Mini Systems, Inc. The heaters were mounted on glass posts to give structural support and also for insulation to minimize heat loss. A sump system was used to remove excess fluid from around the heaters. To help control spray splash-back, angled containment caps were placed over the sump annuli, between the spray nozzles and the heater pedestals. A circular opening at the top of each cap allowed the spray to enter and contact the heater. The positioning of the heater post with respect to the drain sump and containment cap can be seen in Fig. 6. Because the test rig was also used in variable-gravity testing, a wick structure consisting of wire mesh and stainless steel was placed against the inner wall of the cylindrical test chamber to assist with fluid containment.

During testing, temperature data was taken using thermocouples imbedded within the heater pedestal. For the current experiment, only the bottom nozzle was used.

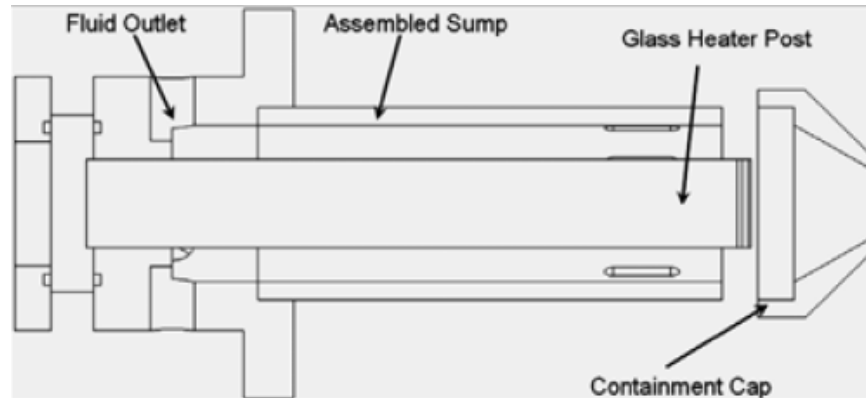


Figure 6. Pedestal and sump arrangement (Yerkes et al., 2006).

The fluid recirculation system consisted of three loops. A flow schematic showing each loop and the instruments contained therein can be seen in Fig. 7. One loop was the test fluid circulation loop, labeled Loop A in Fig. 7, which contained the cooling fluid. The FC-72 circulated through the loop and was sprayed from the nozzle onto the heater surface during testing. The second fluid loop, labeled Loop B in Fig. 7, was a drain loop for the cooling fluid. The purpose of the drain loop was to remove excess fluid from the spray chamber to ensure the chamber never became flooded. The third fluid loop, labeled Loop C in Fig. 7, contained water, whose temperature was controlled using reheaters in the loop. The water was circulated around the chamber to control the saturation temperature and pressure of the FC-72 within the chamber. Tubing in low pressure regions of the fluid loops was composed of plastic, while in regions of higher pressure stainless steel was used. The system was monitored using a data acquisition system, flow meters, pressure transducers, and type E thermocouples.

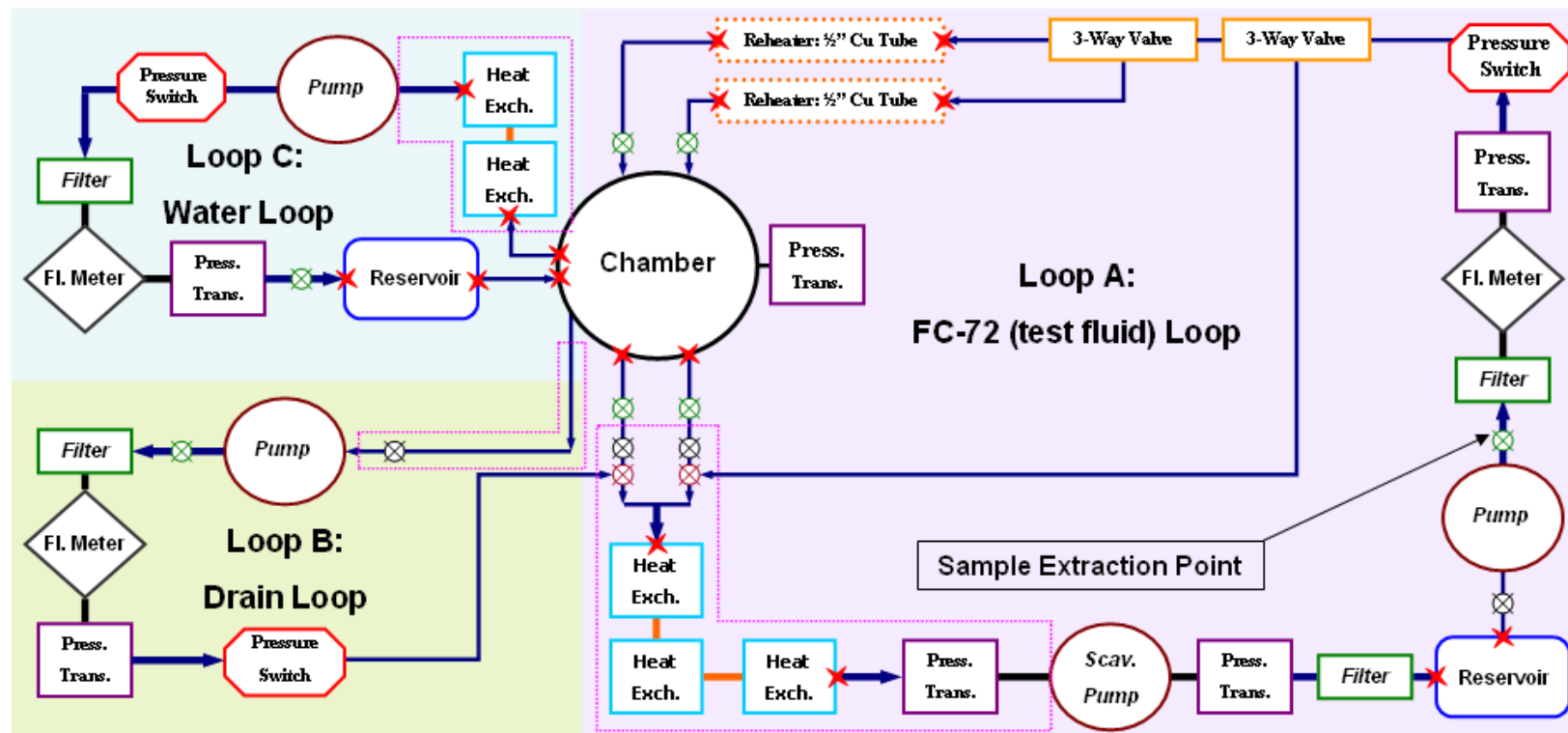


Figure 7. Flow loop schematic for the experimental test rig.

The 0.016 m diameter heater pedestal used in the experiment was similar to that described by Baysinger (2005). However, in the current experiment, a thick film resistor (TFR) heater was used. A total of five layers of material made up the heater pedestal assembly: the TFR heater, two glass wafers, a glass post, and a glass base. The layers, with the exception of the glass base, can be seen in the side view of the heater pedestal shown below in Fig. 8. The grooves in the side of the pedestal allowed space for thermocouple wires in the various pedestal layers.

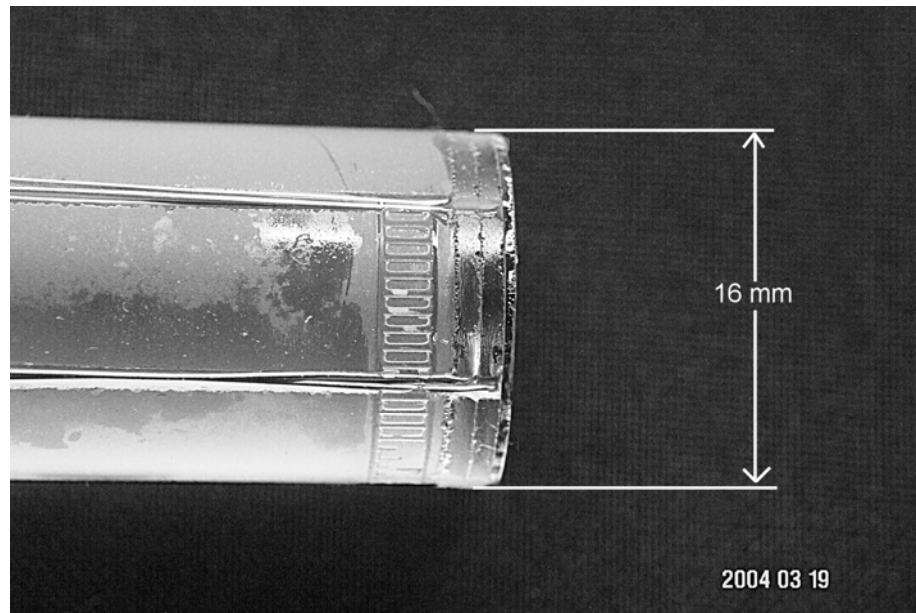


Figure 8. Heater pedestal side view (Yerkes et al., 2006).

The heater consisted of a ceramic substrate, a thick film resistive element, and a glass cover plate. The thicknesses and thermal conductivities of these materials can be seen in Fig. 9. The ceramic substrate forms the base of the heater, while the glass cover plate protects the resistive element.

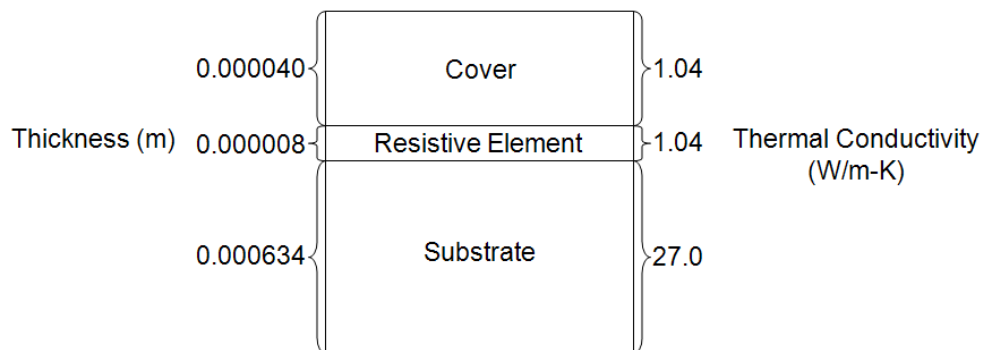


Figure 9. Heater layer dimensions and thermal conductivities (not to scale).

The heater was attached to the first glass wafer using optical cement. That glass wafer was then attached to the second glass wafer, which was attached to the glass post. The whole assembly was then attached to the glass base. The components of the heater pedestal assembly can be seen in Fig. 10, while the fully assembled pedestal can be seen in Fig. 11. The purpose of the glass wafer layers was to allow thermocouple placement at various points in the pedestal. A photograph showing thermocouple placement in the pedestal can be seen in Fig. 12.

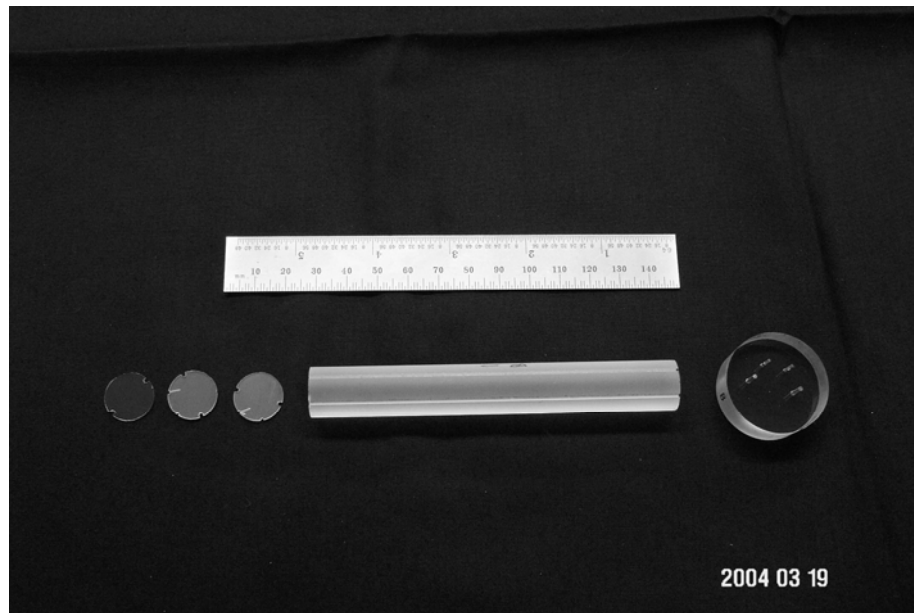


Figure 10. Heater pedestal components (Baysinger, 2005).

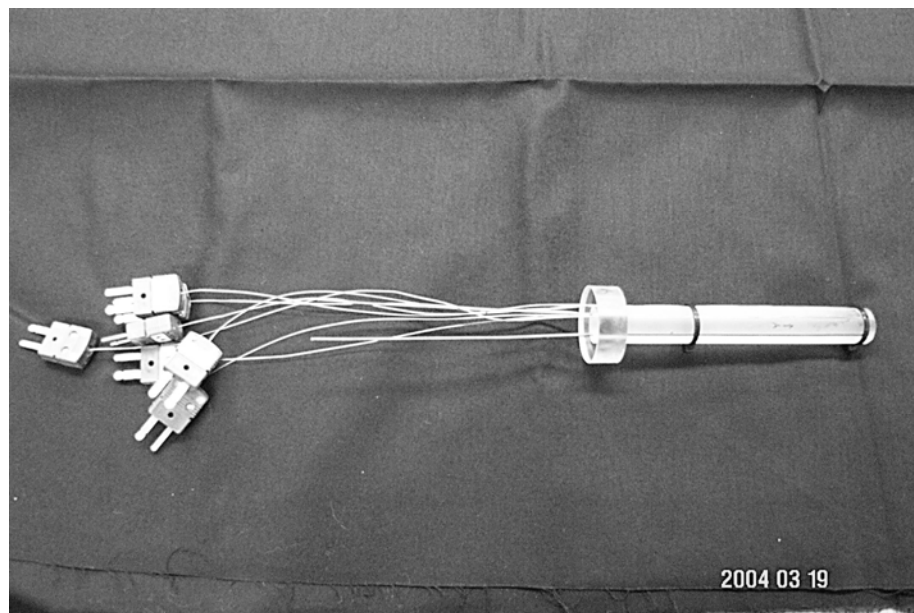


Figure 11. Fully assembled heater pedestal (Yerkes et al., 2006).

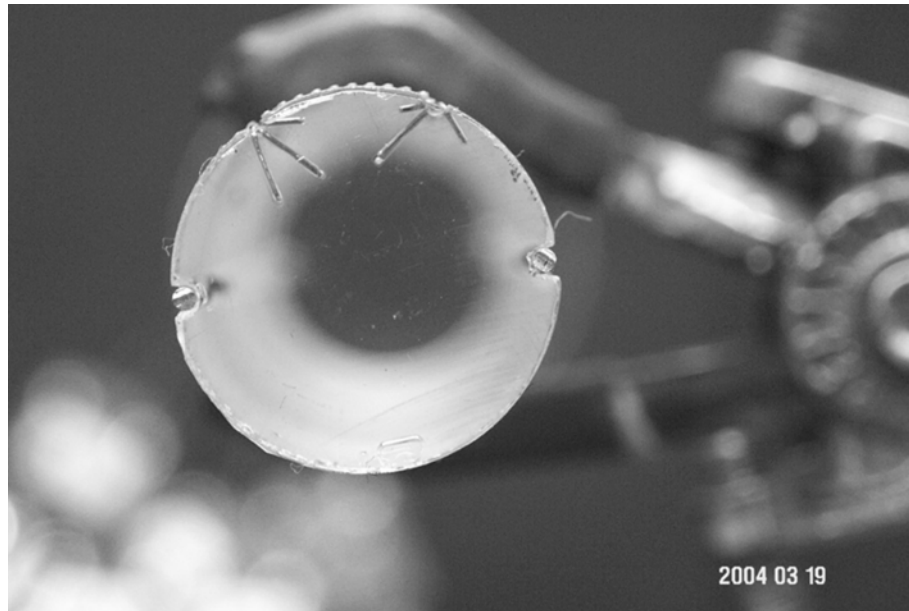


Figure 12. Heater pedestal top view with thermocouples (Yerkes et al., 2006).

To control the amount of air contained within the FC-72 at any given time, several techniques were used. Before the FC-72 loop on the test rig was filled, the fluid was boiled to remove as much air as possible from solution, resulting in fluid that was approximately $C = 4\%$ air by volume. The loop was then filled following the fill procedure outlined in Appendix A. Following the fill, the amount of dissolved air in the loop fluid was determined via a fluid sample. A complete step-by-step procedure for obtaining and analyzing a sample is given in Appendix A. If the amount of air was greater than desired, a Membrana Superphobic membrane filter, Model G628, was used to remove air from the FC-72. The filter can be seen in Fig. 13 and consists of a plastic cylinder with an internal membrane permeable to air, but impermeable to FC-72. Three fittings were incorporated into the filter: One to which a vacuum pump was attached, and two others which allowed the working fluid to pass from the rig, through the filter and return to the rig. As the fluid flowed through the filter, air was removed. If the amount of air in the fluid was less than desired, additional air was bled into the system. The chamber pressure was used as a rough indicator of the amount of air in the system at any given time. If a more specific measure of the amount of air in the system was needed, a fluid sample was taken and tested. Figure 14 shows the rough correlation between the

amount of dissolved air present in the system and the system chamber pressure. The procedure for use of the membrane filter can be found in Appendix A.



Figure 13. Membrane filter used for removal of air from FC-72.

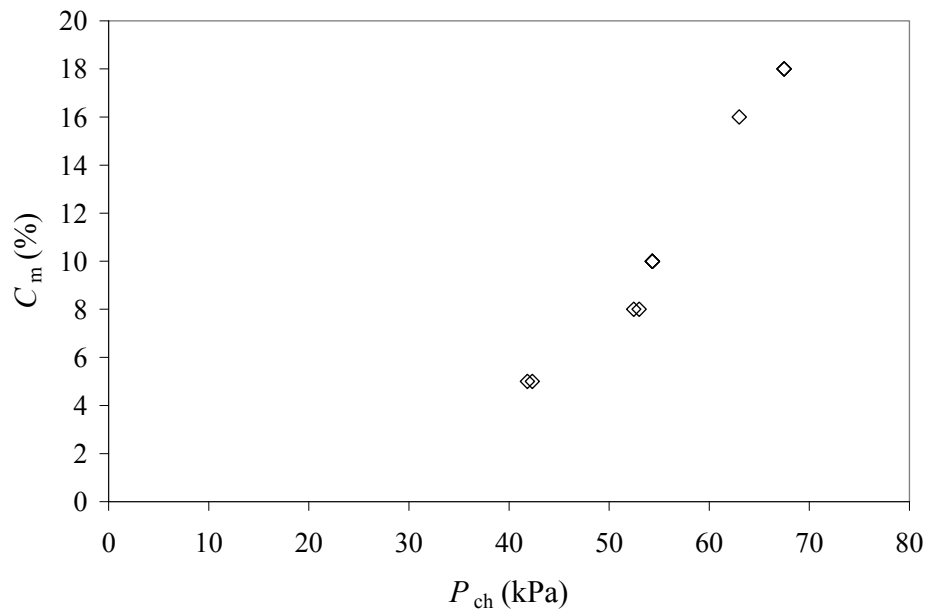


Figure 14. Variation in C_m with P_{ch} .

Before each test run, a sample of FC-72 was taken and tested for air content using a Seaton-Wilson AD-4003 aire-ometer, which can be seen in Fig. 15. These samples were extracted through the fill valves downstream of the reservoir, as shown in the flow loop schematic in Fig. 7. To keep any non-system air from being introduced to the sample, the sample line was purged of air and replaced with working fluid. Each sample

was then pressure-fed to a hypodermic syringe consisting of approximately 5 ml of fluid. The sample volume was less than 1% of the total fill volume of the spray system. During analysis, 1 ml of the sample was used to flush the Aire-ometer liquid line. A 1-ml sample was then placed in the Aire-ometer tube, and the fluid contained within the tube was placed under a slight vacuum, separating the gas contained within the fluid from the fluid itself. Once the gas and fluid were separated, a reading was taken. Three 1-ml samples were analyzed, at a given air content condition, to ensure repeatability. After multiple samples were taken, depleting approximately 20 to 30 ml of fluid volume in the flow loop, the test rig was topped off using additional degassed fluid.



Figure 15. Aire-ometer used for measuring dissolved gas concentration in fluids.

During testing, several experimental parameters were controlled to obtain the desired testing conditions. Such parameters included the chamber pressure, P_{ch} , the amount of subcooling, ΔT_{sc} , the flow rate, \dot{V} , and the heat rate, \dot{Q} . The chamber pressure, P_{ch} , was controlled during testing and adjusted if necessary using a reheater

incorporated into the water loop. A reheater in the FC-72 loop was used to raise the FC-72 liquid temperature at the nozzle to achieve the desired amount of subcooling, ΔT_{sc} .

The flow rate, \dot{V} , was set to the desired amount and adjusted as necessary throughout the experiment. Once the system was determined to be in equilibrium, the test was started. Tests were conducted by supplying voltage to the thick film resistor heater starting at $Q = 5$ W and incrementing the heat input by 5 W every 2 minutes, allowing the system to reach steady state at each heater increment. For data evaluation purposes, steady state was defined to be reached when the change in heat interface temperature with respect to time was less than 0.05 °C/s. Q_{CHF} was defined to be 2.5 W less than the heater power load at which CHF appeared to occur. Such a method for determination of Q_{CHF} was developed to account for the fact that the actual power at which CHF occurred may have been at a level lower than the final power setting, but higher than the previous power setting. Once CHF was reached, the heater power was turned off and the test was terminated.

III. Empirical Mathematical Relationship

For data reduction purposes, it was necessary to determine the surface temperature of the heater. Because no thermocouple was placed on the surface of the heater, no direct method for obtaining the surface temperature existed. As a result, the temperature was calculated using the heater interface temperature, a location at which a thermocouple reading was obtainable. To derive an equation for the surface temperature in terms of the interface temperature, the conservation of energy equation was used, along with interface boundary conditions for each of the three heater sections. The geometry of the thick film resistor (TFR) heater, along with the heat transfer can be seen in Fig. 16.

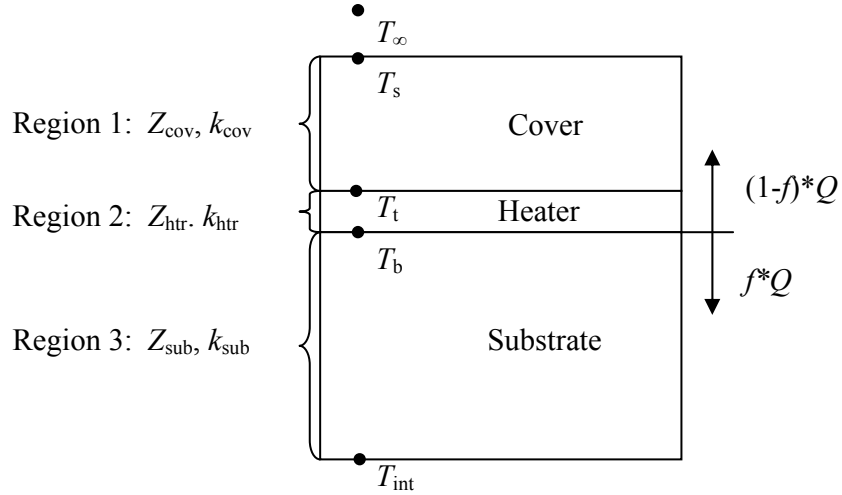


Figure 16. Thick film resistor heater schematic (not to scale).

In Fig. 16, the power produced by the resistive heater is denoted by Q , while f is the fraction of heat transferred down the pedestal. The value of f was assumed to be 1.5%, an intermediate value in the range specified in previous papers (Baysinger et al. 2005; Baysinger 2005). The heater was divided into three regions, and each region was analyzed using the energy equation as the governing equation, with the interface fluxes and temperatures as the boundary conditions.

Region 1, the cover, can be seen in Fig. 17 below, along with the flux boundary conditions and interface temperatures. One-dimensional steady state heat conduction was assumed, with no heat generation.

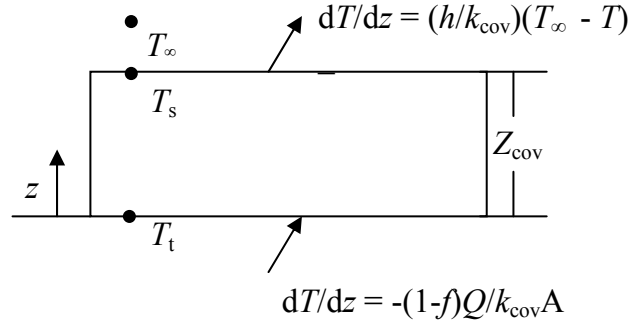


Figure 17. Cover geometry with boundary conditions.

The conservation of energy equation and boundary conditions for Region 1 are:

$$\frac{d^2 T}{dz^2} = 0 \quad (1)$$

$$\text{at } z = Z_{\text{cov}}, \frac{dT}{dz} = \frac{h}{k_{\text{cov}}} (T_{\infty} - T_s) \quad (2)$$

$$\text{at } z = 0, \frac{dT}{dz} = \frac{-(1-f)Q}{k_{\text{cov}} A} \quad (3)$$

The first boundary condition was due to convection between the upper surface and the cooling fluid. The second boundary condition was due to conduction from the heater through the cover.

Upon integration of Eqn. (1) and application of the boundary conditions, the equation for T_s in terms of T_t was determined to be:

$$T_s = -\frac{(1-f)QZ_{\text{cov}}}{k_{\text{cov}} A} + T_t \quad (4)$$

Region 2, the heater, can be seen in Fig. 18 below, along with the flux boundary conditions and interface temperatures. One-dimensional steady state heat conduction was assumed, with heat generation.

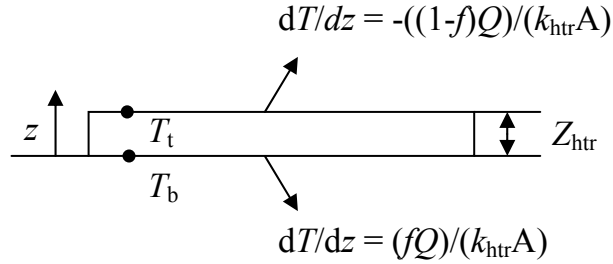


Figure 18. Heater geometry with boundary conditions.

The equation for Region 2 can be seen in Eqn. (5) below, along with the boundary conditions in Eqns. (6) and (7):

$$\frac{d^2 T}{dz^2} + \frac{g}{k_{htr}} = 0 \quad (5)$$

$$\text{at } z = Z_{htr}, \frac{dT}{dz} = -\frac{(1-f)Q}{k_{htr}A} \quad (6)$$

$$\text{at } z = 0, \frac{dT}{dz} = \frac{fQ}{k_{htr}A} \quad (7)$$

The first boundary condition was due to conduction from the heater to the cover, while the second boundary condition was due to conduction from the heater to the substrate.

Upon integration of the equation and application of the boundary conditions, the equation for T_t in terms of T_b was determined to be:

$$T_t = \frac{QZ_{htr}}{Ak_{htr}} \left(f - \frac{1}{2} \right) + T_b \quad (8)$$

Region 3, the substrate, can be seen in Fig. 19 below, along with the flux boundary conditions and interface temperatures. One-dimensional steady state heat conduction was assumed, with no heat generation.

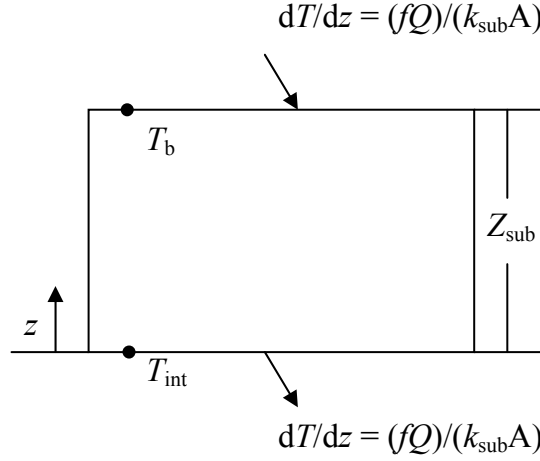


Figure 19. Substrate geometry with boundary conditions.

The equation for Region 3 can be seen in Eqn. (9) below, along with the boundary conditions in Eqns. (10) and (11):

$$\frac{d^2 T}{dz^2} = 0 \quad (9)$$

$$\text{at } z = 0, \frac{dT}{dz} = \frac{fQ}{k_{sub} A} \quad (10)$$

$$\text{at } z = Z_{sub}, \frac{dT}{dz} = \frac{fQ}{k_{sub} A} \quad (11)$$

The first boundary condition was due to conduction from the heater to the substrate, while the second boundary condition was due to conduction from the substrate to the glass pedestal.

Upon integration of the equation and application of the boundary conditions, the equation for T_b in terms of T_{int} was determined to be:

$$T_b = \frac{fQ}{k_{sub}A} Z_{sub} + T_{int} \quad (12)$$

Combining the three equations yields the surface temperature in terms of the interface temperature:

$$T_s = \frac{-(1-f)}{k_{cov}A} QZ_{cov} + \frac{QZ_{htr}}{Ak_{htr}} \left(f - \frac{1}{2} \right) + T_{int} + \frac{fQ}{k_{sub}A} Z_{sub} \quad (13)$$

The surface temperature from Eqn. (13) was used for data reduction purposes.

Upon observation of data obtained through various experimental test runs, it was theorized that an empirical mathematical model for heat flux curves could be developed which would take into account subcooling, sensible heat, CHF, and volumetric flow rate. Heat flux was plotted as a function of wall superheat, the temperature drop from the surface of the heater to the saturation temperature: $\Delta T = T_s - T_{sat}$. A second-order mathematical relationship allowing determination of surface heat flux for a given flow rate and surface temperature was developed. Figure 20 shows a theoretical heat flux curve with the key points of interest noted. Such key points are ΔT_{sc} : the point at which $T_s - T_{sat} = T_f - T_{sat}$, $q(\Delta T=0)$: the heat flux at which saturation temperature is reached, and q_{CHF} and ΔT_{CHF} , corresponding to the point at which CHF is reached.

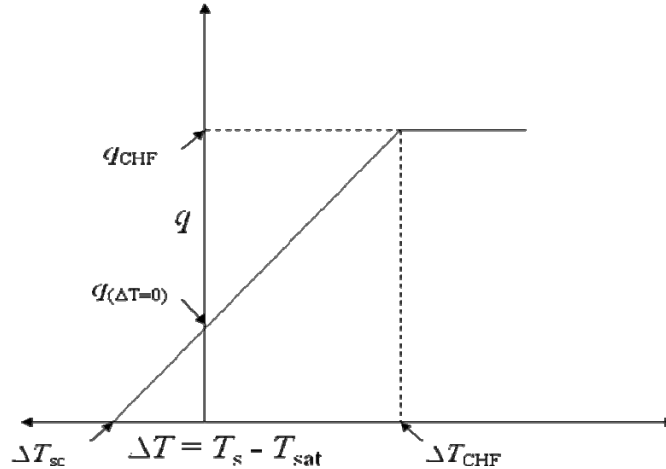


Figure 20. q vs ΔT showing key points for coefficient determination.

To develop the empirical relationship, the surface heat flux, q , was assumed to be a second-order function of ΔT . Such an assumption was made as a result of the shape of

the curve when heat flux was plotted as a function of wall superheat. As a result, the general equation for heat flux was:

$$q = a\Delta T^2 + b\Delta T + c \quad (14)$$

The coefficients a , b , and c were determined using ΔT_{sc} , along with the volumetric flow rate, \dot{V} , and functional relationships for the sensible heat, $q_{(\Delta T=0)}$, the critical heat flux, q_{CHF} , and the ΔT at which critical heat flux occurs, ΔT_{CHF} .

The functional relationships were developed by plotting each of the three variables, $q_{(\Delta T=0)}$, q_{CHF} , and ΔT_{CHF} , against flow rate for experimental data at three different values for \dot{V} . After the plots were made, a second-order polynomial fit was used for each variable to obtain a relationship as a function of \dot{V} . Figures 21 through 23 show the three functional relationships for $q_{(\Delta T=0)}$, q_{CHF} , and ΔT_{CHF} with volumetric flow rate, \dot{V} , for the case of $C = 10\%$, $10 \leq \Delta T_{sc} \leq 12^\circ\text{C}$, and $\dot{V} = 6.31, 8.41, \text{ and } 10.5 \text{ cm}^3/\text{s}$ (6.0, 8.0, and 10.0 gph).

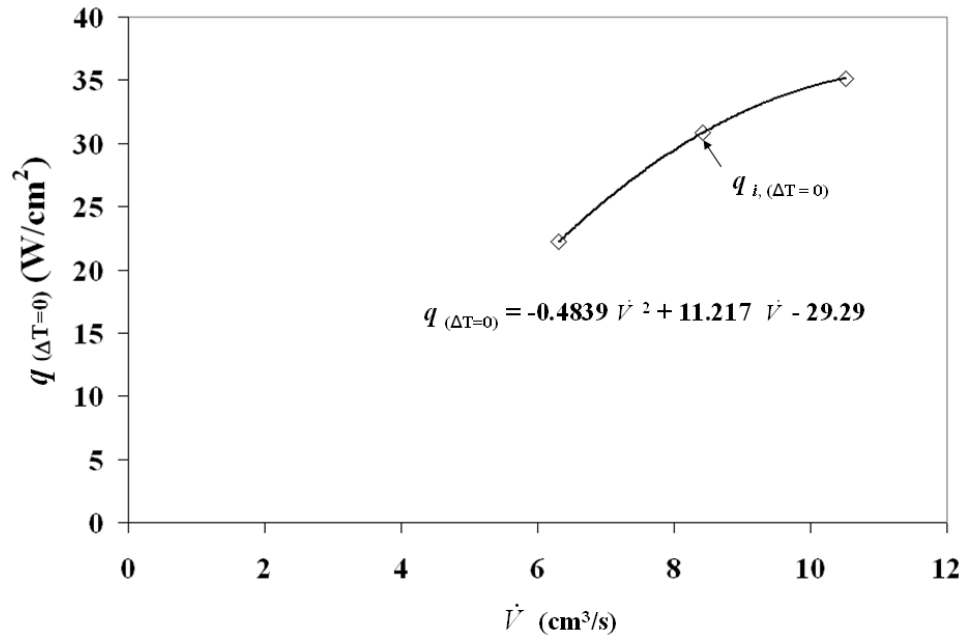


Figure 21. Functional relationship equations for $q_{(\Delta T=0)}$; $C_m = 10\%$, $10 \leq \Delta T_{sc} \leq 12^\circ\text{C}$, and $\dot{V} = 6.31, 8.41, \text{ and } 10.5 \text{ cm}^3/\text{s}$.

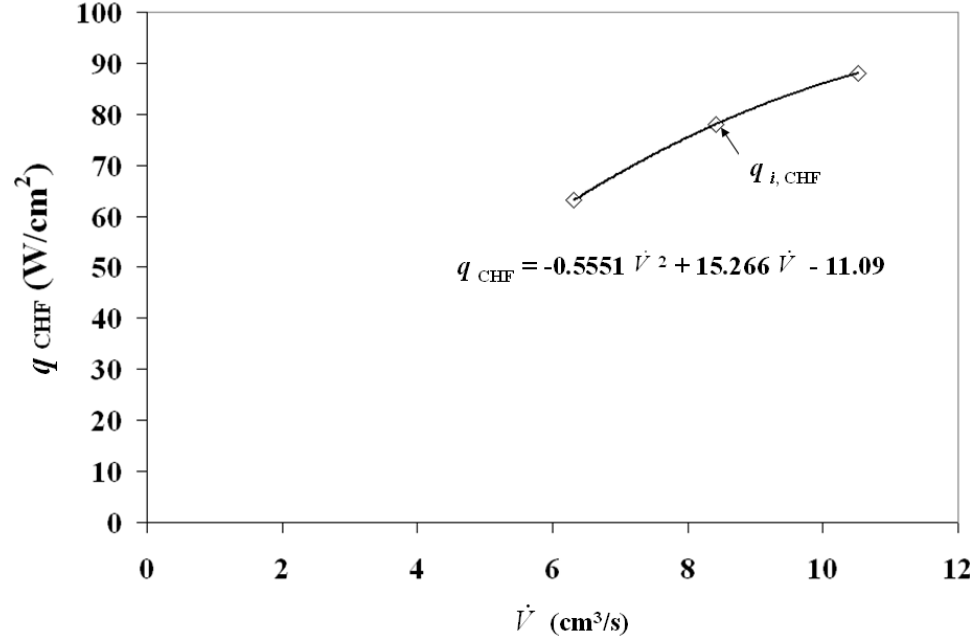


Figure 22. Functional relationship equations for q_{CHF} ; $C_m = 10\%$, $10 \leq \Delta T_{sc} \leq 12^\circ C$, and $\dot{V} = 6.31, 8.41, \text{ and } 10.5 \text{ cm}^3/s$.

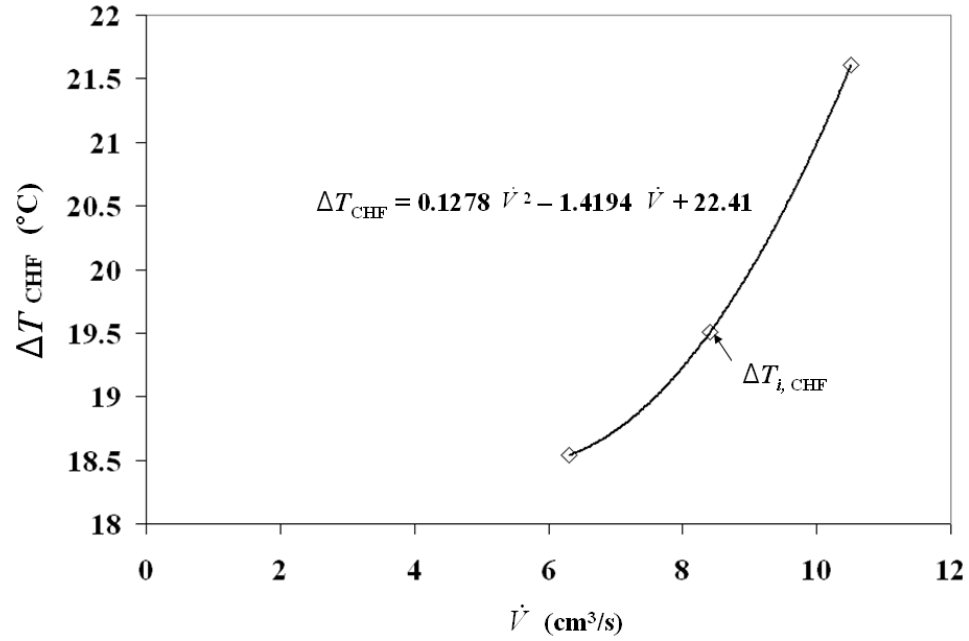


Figure 23. Functional relationship equations for ΔT_{CHF} ; $C_m = 10\%$, $10 \leq \Delta T_{sc} \leq 12^\circ C$, and $\dot{V} = 6.31, 8.41, \text{ and } 10.5 \text{ cm}^3/s$.

Following determination of the functional relationships, the coefficients of the general equation were determined. First, the coefficient c was determined using $q_{(\Delta T=0)}$:

$$q_{(\Delta T=0)} = a(0)^2 + b(0) + c \quad (15)$$

$$c = q_{(\Delta T=0)} \quad (16)$$

The general equation then became:

$$q = a\Delta T^2 + b\Delta T + q_{(\Delta T=0)} \quad (17)$$

The coefficients a and b were then evaluated using the following simultaneous equations:

$$q_{CHF} = a(\Delta T_{CHF})^2 + b(\Delta T_{CHF}) + q_{(\Delta T=0)} \quad (18)$$

and

$$0 = a(\Delta T_{sc})^2 + b(\Delta T_{sc}) + q_{(\Delta T=0)} \quad (19)$$

Following algebraic manipulation, coefficient a was determined to be

$$a = - \left\{ \frac{q_{(\Delta T=0)}}{\Delta T_{sc}^2} + \frac{\left[q_{CHF} + \frac{q_{(\Delta T=0)}\Delta T_{CHF}^2}{\Delta T_{sc}^2} - q_{(\Delta T=0)} \right]}{\Delta T_{sc} \left[\Delta T_{CHF} - \frac{\Delta T_{CHF}^2}{\Delta T_{sc}} \right]} \right\} \quad (20)$$

and coefficient b became

$$b = \left\{ \frac{q_{CHF} + \frac{q_{(\Delta T=0)}\Delta T_{CHF}^2}{\Delta T_{sc}^2} - q_{(\Delta T=0)}}{\left[\Delta T_{CHF} - \frac{\Delta T_{CHF}^2}{\Delta T_{sc}} \right]} \right\} \quad (21)$$

Upon determination of the coefficients, Eqn. (17) can be used to predict heat flux behavior of a cooled surface based on flow rate and amount of subcooling.

IV. Results and Discussion

The objective of the current experiment was to determine the effect of variation in dissolved air content in a spray cooling system. The dissolved air was measured directly by volume using an aire-ometer. As opposed to direct measurement, work performed by previous researchers has involved determination of dissolved air amounts using partial pressures and Henry's law.

McMurry and Fay (1995), state that the gas solubility of a liquid is proportional to the partial pressure of the gas over the solution,

$$M^* = HP_g \quad (22)$$

where H is Henry's constant, and varies depending upon the working fluid and temperature. Henry's law is generally applied to a closed, steady state system. McMurry and Fay (1995) described Henry's law and its effects on a system. When a system is at equilibrium at a given pressure, equal numbers of gas particles are entering and leaving the solution. If the pressure in the system is increased, more gas particles are forced to enter the solution than to leave it. When a new equilibrium is established, more gas particles are in the liquid than were previously, but the gas particles entering the solution and those leaving are once again equal. Henry's law is applicable to the system only when it is in equilibrium.

Another notable characteristic of Henry's law is that it is only applicable to dilute gas-liquid solutions. Çengel and Boles (1989) characterize dilute gas-liquid solutions as liquids with a small amount of gas dissolved in them. Unfortunately, a better description of a dilute solution was not found. Çengel and Boles did mention the case of ammonia in water as being one to which Henry's law was not applicable, because ammonia was too soluble in water. According to the Spacecraft Water Exposure Guidelines for Selected Contaminants (2007), ammonia is soluble in water up to 31% at 25°C.

Also important to note is the temperature dependence of Henry's constant for a given gas-fluid mixture. According to Smith and Harvey (2007), Henry's constant has significant non-linear temperature dependence such that in some cases, a temperature variation of 10°C can cause a change in Henry's constant by as much as a factor of two. Henry's constant typically increases with temperature up to a certain maximum, then decreases with further increases in temperature.

During testing, samples of FC-72 were taken for each data set to determine the air content as a volume fraction, $C_m = [V_{\text{air}} / (V_{\text{FC}} + V_{\text{air}})] \times 100$, while the spray chamber was at saturation conditions with an ambient temperature of $T_{\text{amb}} = 20.5 \pm 0.5^\circ\text{C}$. Upon determination of C_m , that value was converted to a volume ratio, $C_m^* = V_{\text{air}} / V_{\text{FC}}$, by the following equation:

$$C_m^* = \frac{\left(\frac{C_m}{100}\right)}{1 - \left(\frac{C_m}{100}\right)} \quad (23)$$

To implement Henry's law, the volume ratio was converted to a molar ratio, as shown below:

$$M_m^* = C_m^* \left(\frac{\rho_{\text{air},\text{ref}}}{\rho_{\text{FC},\text{ref}}} \right) \left(\frac{m_{\text{FC}}}{m_{\text{air}}} \right) \quad (24)$$

Control of the spray chamber pressure was used to maintain a specific fluid saturation temperature during testing. This was done in an attempt to ensure comparability of test results. Although control of the chamber pressure was attempted, identical thermodynamic conditions within the chamber for each test run could not be ensured. As a result, the air content in the fluid being sprayed onto the heater during a test run may have differed from the air content in the fluid being sprayed onto the heater when a fluid sample was taken prior to testing. A method for obtaining a corrected volume ratio, taking into consideration pressure variations during sampling and testing, was developed. The pressure-corrected volume ratio, C^* , was obtained using a ratio of Henry's law:

$$\frac{M_m^* = HP_{g,ref}}{M^* = HP_g} \quad (25)$$

which simplified to give:

$$M^* = \frac{M_m^* P_g}{P_{g,ref}} \quad (26)$$

The above equation then had to be converted back to volume ratios to give the desired corrected volume ratio. Equation (27) gives the corrected molar ratio in terms of the corrected volume ratio, similar to Eqn. (24) for the measured values.

$$M^* = C^* \left(\frac{\rho_{air}}{\rho_{FC}} \right) \left(\frac{m_{FC}}{m_{air}} \right) \quad (27)$$

Using Eqn. (26) in conjunction with Eqn. (24) and Eqn. (27), the corrected volume ratio was determined to be:

$$C^* = \frac{C_m^* P_g \left(\frac{\rho_{FC}}{\rho_{air}} \right)}{P_{g,ref} \left(\frac{\rho_{FC,ref}}{\rho_{air,ref}} \right)} \quad (28)$$

The corrected volume ratio, C^* , was then converted back to a volume fraction, C .

Figure 24 shows a typical experimental heater temperature trace with time. Voltage was supplied to the thick film resistor heater starting at $Q = 5$ W. The heat input was incremented by 5 W every 2 minutes, allowing the system to reach steady state at each heater increment. When the change in heater interface temperature with respect to time was less than 0.05 °C/s, steady state was considered to have been reached. Critical heat flux was considered to have been reached when a dramatic increase in T_{int} indicated loss of sufficient heater cooling, and the temperature cut-off switch on the heater power was triggered at $T_{int} > 130$ °C. The steady state increments for several power settings can be seen in Fig. 24 below, along with the temperature spike indicating CHF.

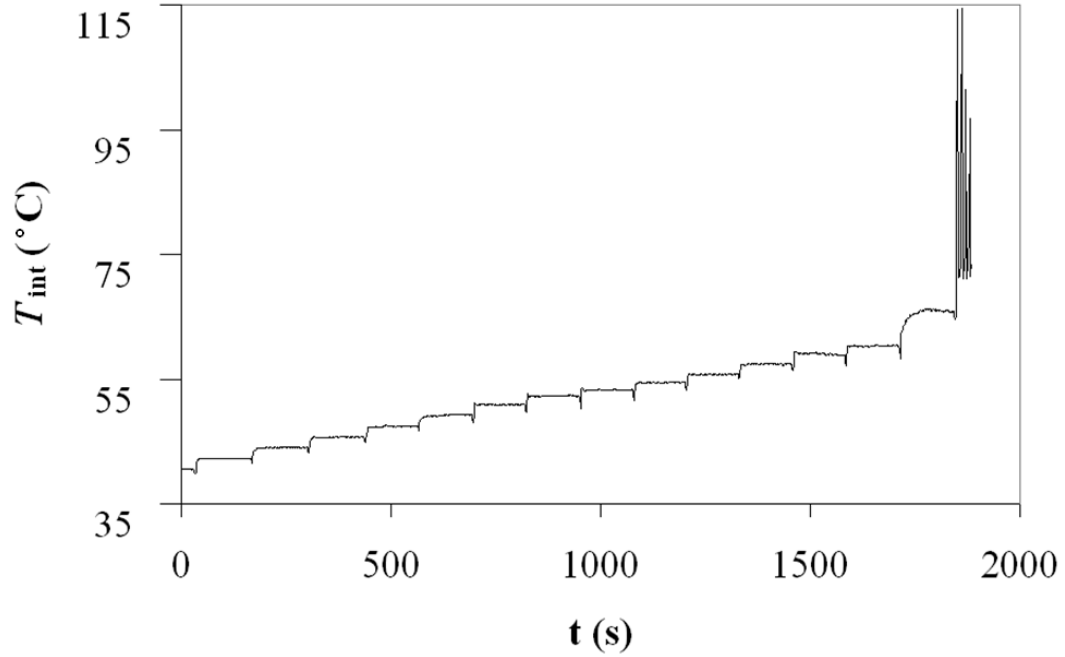


Figure 24. Heater temperature variation with time.

To evaluate the effect of varying C on critical heat flux, test runs were grouped according to those with statistically comparable \dot{V} , ΔT_{sc} and P_{ch} . Although statistical comparability was the goal, some of the variables, notably P_{ch} , were difficult to control. As a result, a few of the parameters in the test cases did not fall within statistical bounds of each other. Groupings were made such that possible trends could be identified. Four sets of three test runs were found to be comparable, as shown in Table 1. Tests conducted with little to no variation in the experimental parameters, \dot{V} , ΔT_{sc} , P_{ch} , and C_m , were seen to yield repeatable results. The heat flux curves in such cases were very similar, and CHF occurred at a similar heat load.

Set	Run	\dot{V} (cm ³ /s)	ΔT_{sc} (°C)	P_{ch} (kPa)	C_m (%)	C (%)	q_{CHF} (W/cm ²)
1	a	6.35 ± 0.074	11.40 ± 0.40	57.78 ± 0.97	8 ± 2	8.04 ± 2.1	65.18 ± 1.8
	b	6.28 ± 0.063	11.01 ± 0.40	57.23 ± 0.97	10 ± 2	10.00 ± 2.1	63.36 ± 1.8
	c	6.28 ± 0.053	11.33 ± 0.40	72.81 ± 1.0	18 ± 2	18.12 ± 2.2	62.83 ± 1.8
2	a	8.54 ± 0.13	8.91 ± 0.90	60.12 ± 2.1	5 ± 2	5.15 ± 3.7	69.48 ± 1.8
	b	8.50 ± 0.095	10.40 ± 0.80	79.78 ± 2.1	10 ± 2	10.29 ± 3.3	69.34 ± 1.8
	c	8.39 ± 0.24	8.22 ± 0.40	80.40 ± 1.2	16 ± 2	16.16 ± 2.1	60.72 ± 1.8
3	a	8.81 ± 0.15	11.86 ± 0.60	40.27 ± 1.3	5 ± 2	5.00 ± 2.2	71.64 ± 1.8
	b	8.37 ± 0.16	11.94 ± 0.50	59.71 ± 1.2	10 ± 2	10.00 ± 2.1	76.84 ± 1.8
	c	8.42 ± 0.095	12.18 ± 0.40	76.60 ± 1.1	18 ± 2	18.12 ± 2.2	76.92 ± 1.8
4	a	10.50 ± 0.063	12.41 ± 0.50	61.16 ± 1.2	8 ± 2	8.02 ± 2.1	91.09 ± 1.8
	b	10.43 ± 0.58	12.67 ± 0.40	61.64 ± 1.0	10 ± 2	10.00 ± 2.1	90.64 ± 1.8
	c	10.53 ± 0.063	12.83 ± 0.40	79.29 ± 1.2	18 ± 2	18.12 ± 2.2	87.35 ± 1.8

Table 1. Experimental results including precision error only.

Experimental data showing heat flux curves for each of the data sets in Table 1 can be seen in Figures 25 through 28. Each plot shows a distinct heat flux curve for each test run in each set. Comparing all four figures, no trend can be seen with varying C_m . For example, in Fig. 25, the test with the lowest C_m shows the lowest values for q , while in Fig. 26, the test with the highest C_m shows the lowest values for q .

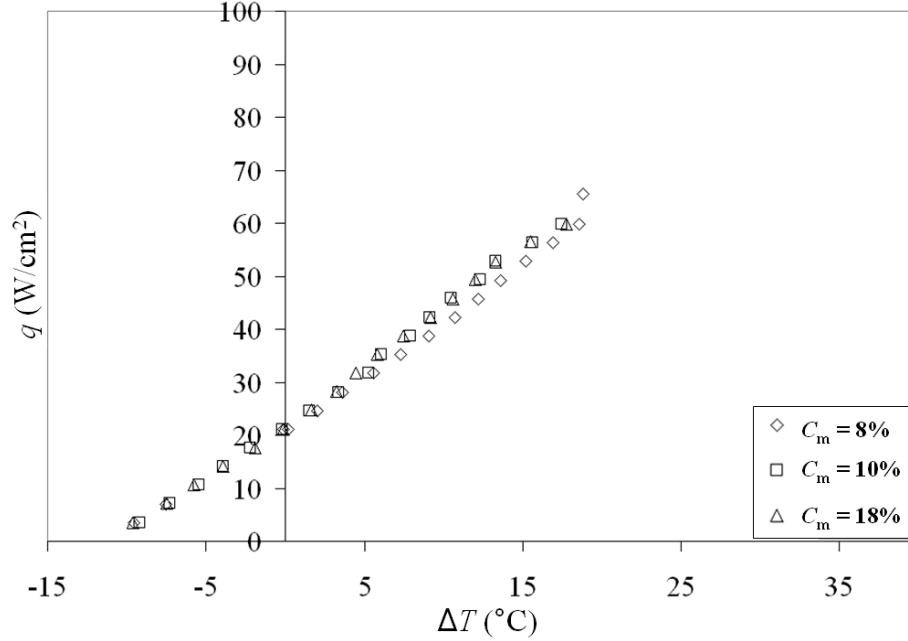


Figure 25. q versus ΔT for Set 1.

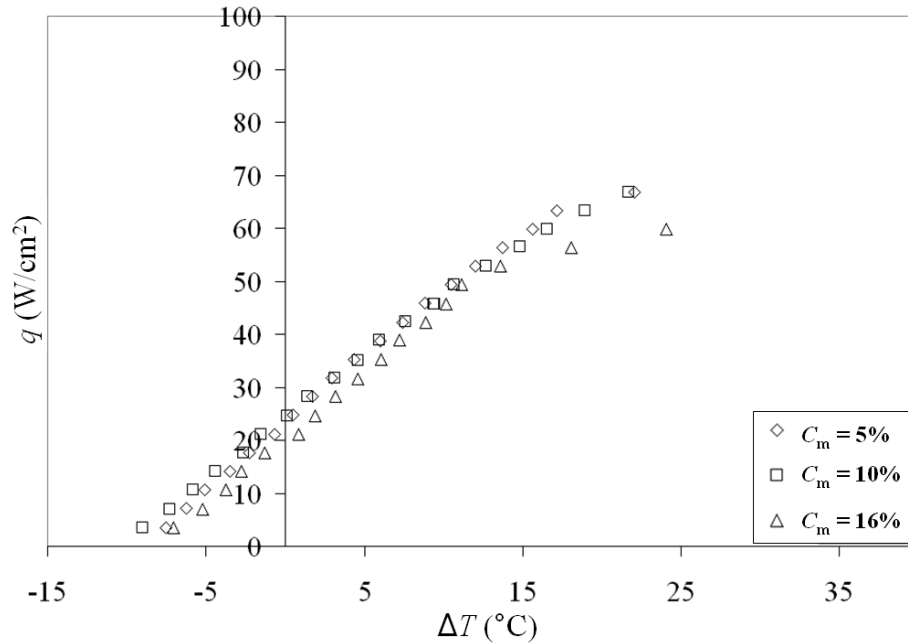


Figure 26. q versus ΔT for Set 2.

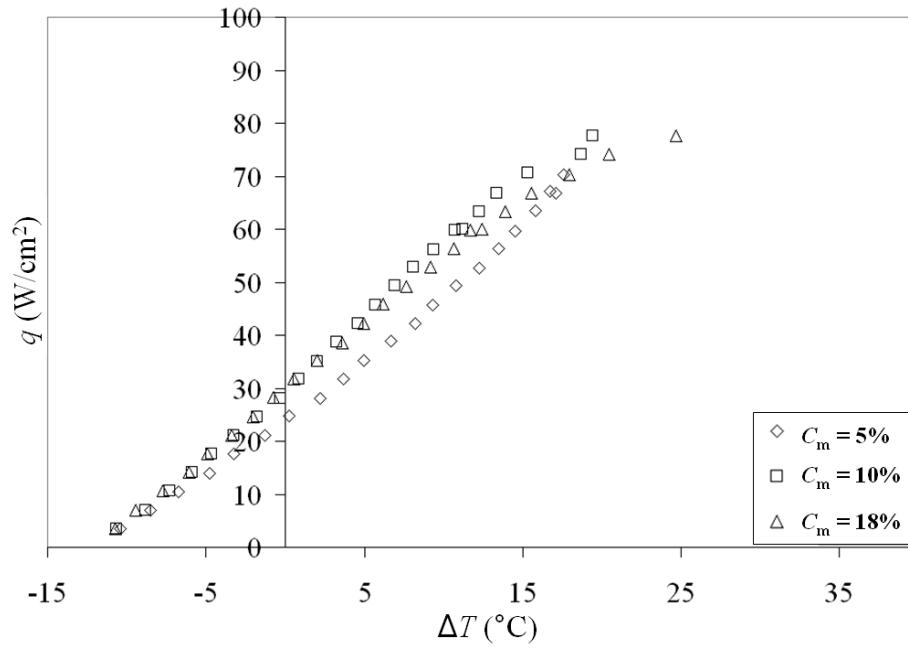


Figure 27. q versus ΔT for Set 3.

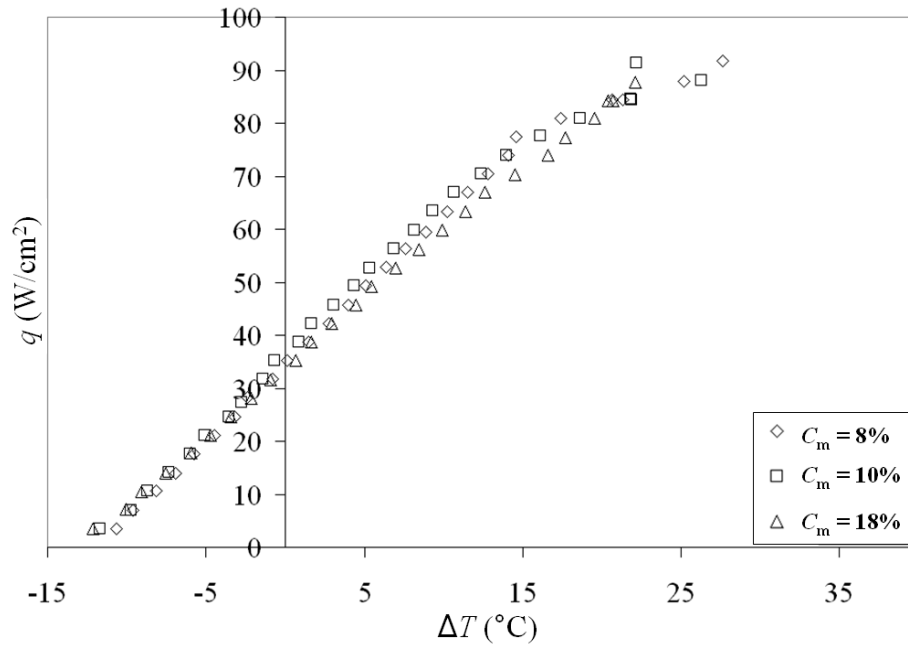


Figure 28. q versus ΔT for Set 4.

Some of the results shown in Table 1 were to be expected. Comparison of Sets 1, 3 and 4 shows an increase in CHF with flow rate, as is consistent with previous findings by Estes and Mudawar (1995) and Rybicki and Mudawar (2006). Comparison of Sets 2 and 3 shows an increase in CHF with subcooling, as is consistent with previous findings

by Lin and Ponnappan (2003), Horacek et al. (2003, 2004), and Rybicki and Mudawar (2006).

It can be seen from Table 1 that no statistical variation in CHF occurred in Set 1 of the test runs. While Runs 1a and 1b did not have statistically different air content values, the air content value for Run 1c was notably higher. From previous research, one would assume that the higher air content would result in a higher CHF (Milke et al., 1997; Horacek et al., 2003, 2004). In fact, the higher P_{ch} value for Run 1c would also be expected to cause an increase in CHF. Such a result was not observed. The values for P_{ch} and C increased for each run in Set 2, which would be expected to cause consistently increasing values for CHF. Run 2c actually showed a decrease in CHF when compared with Runs 2a and 2b, which were statistically similar. A possible explanation for the lower CHF value could be the slightly lower flow rate in Run 2c, coupled with a slightly larger than normal error. CHF values for Runs 3b and 3c were slightly higher than those for Run 3a. The increase between Runs 3a and 3b could be explained by the increases in P_{ch} and C . However, P_{ch} and C also increased from Run 3b to Run 3c, and no corresponding increase in CHF was observed. In Set 4, CHF values for Runs 4a and 4b were similar, which was to be expected, as they had statistically similar values for C and P_{ch} . In Run 4c, however, CHF decreased, which was counterintuitive, as both C and P_{ch} were statistically higher.

There was no significant increase in CHF when P_{ch} was controlled. A possible explanation could be that the air content values did not cover a wide range. In each set of test runs, such an explanation could be considered when comparing Run a and Run b, or Run b and Run c. However, comparison of Run a and Run c should include a variation in C large enough to allow observation of effects as a result of that variable. The only case in which the value for q_{CHF} increased for Run c when compared with Run a was that for Set 3. In every other set, the CHF value for Run c was either equivalent to, or less than that for Run a.

The attempt to control P_{ch} could have impacted CHF values and minimized the effect of C . In previous studies, pressure was not controlled; it was simply allowed to vary with varying air content (Lin and Ponnappan, 2003; Horacek et al., 2003, 2004). The attempt at control over that particular parameter could have led to a change in the

effect on CHF. Perhaps in previous studies the effect assumed to be caused by variation in C was actually more directly caused by variation in pressure. To determine which variable had a more direct effect on CHF, further investigation would be needed. A set of tests involving constant C values with varying P_{ch} would need to be run, and the results compared. If CHF was seen to increase with increasing P_{ch} , it would be reasonable to assume that saturation pressure had more of an effect on critical heat flux than did air content. Figure 29 illustrates the fact that there was no consistent trend in CHF as a function of C .

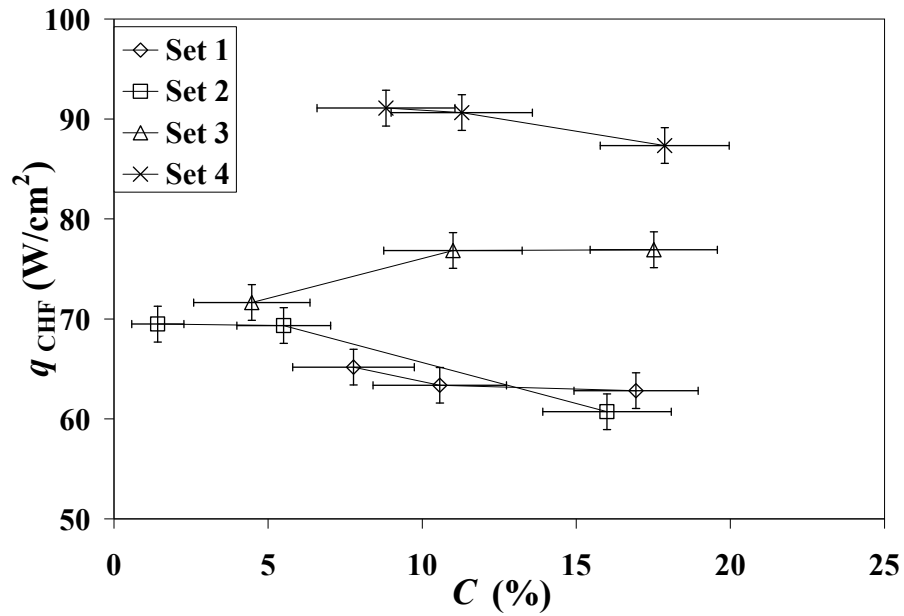


Figure 29. Critical heat flux (CHF) with varying air content for volume-percent.

In an attempt to allow direct comparison between results found in the current research and those found by previous researchers, an effort was made to determine air content using both the aire-ometer, with direct fluid samples, and Henry's law, with partial pressures. For each approach, values for M_m^* and M^* were obtained for comparison.

The equation used to calculate M_m^* using C_m^* can be seen below.

$$M_m^* = C_m^* \left(\frac{\rho_{air,ref}}{\rho_{FC,ref}} \right) \left(\frac{m_{FC}}{m_{air}} \right) \quad (29)$$

The equation for $\rho_{FC,ref}$ was taken from manufacturer information (3M, 2000), with temperature in °C and density in kg/m³.

$$\rho_{FC,ref} = 1740 - 2.61(T_{ch,ref}) \quad (30)$$

$T_{ch,ref}$ was taken as the temperature in the chamber when a fluid sample was taken. The density of air was calculated using the ideal gas law.

$$\rho_{air,ref} = \frac{P_{g,ref}}{R(T_{ch,ref})} \quad (31)$$

The measured partial pressure was determined using Eqn. (32):

$$P_{g,ref} = P_{tot,ref} - P_{sat,ref} \quad (32)$$

$P_{tot,ref}$ was taken as the pressure in the chamber when a fluid sample was taken, while $P_{sat,ref}$ was taken as the vapor pressure corresponding to $T_{ch,ref}$. The equation for $P_{sat,ref}$ was taken from FC-72 manufacturer information (3M, 2000), with temperature in °C, and pressure in kPa.

$$P_{sat,ref} = \frac{\left(10^{\frac{9.729 - \frac{1562}{T_{ch,ref} + 273}}}{1000} \right)}{1000} \quad (33)$$

The equations used to calculate M^* using C^* , were very similar to Eqns. (29) – (33), and can be seen below.

$$M^* = C^* \left(\frac{\rho_{air}}{\rho_{FC}} \right) \left(\frac{m_{FC}}{m_{air}} \right) \quad (34)$$

$$\rho_{FC} = 1740 - 2.61T_{ch} \quad (35)$$

$$\rho_{air} = \frac{P_g}{R(T_{ch})} \quad (36)$$

$$P_g = P_{tot} - P_{sat} \quad (37)$$

$$P_{sat} = \frac{\left(10^{\frac{9.729 - \frac{1562}{T_{ch} + 273}}}{1000} \right)}{1000} \quad (38)$$

P_{tot} was the average chamber pressure over the test run, and P_{sat} was the vapor pressure corresponding to T_{ch} , which was the average chamber temperature over the test run.

The measured molar ratio using Henry's law was calculated using a value for Henry's constant for air in FC-72 from Horacek et al. (2003): $H = 5.4 \times 10^{-5}$ mole/mole-kPa for $31^\circ\text{C} < T < 60^\circ\text{C}$. Although the current experimental temperature values fell outside of the temperature range specified, this value was used for calculation purposes because no other value for Henry's constant for air in FC-72 could be found in the literature. The equations used to calculate M_m^* and M^* using Henry's law can be seen below.

$$M_m^* = H(P_{g,ref}) \quad (39)$$

$$M^* = HP_g \quad (40)$$

The molar ratios calculated using the measured air content and Henry's law for each test run can be seen in Table 2.

Set	Run	M^* from C_m^*		M^* from Henry's law	
		$(M^*)_m$	M^*	$(M^*)_m$	M^*
1	a	$(1.93 \pm 0.54)E-5$	$(2.02 \pm 0.57)E-5$	$(146 \pm 1.9)E-5$	$(153 \pm 5.7)E-5$
	b	$(2.24 \pm 0.57)E-5$	$(2.51 \pm 0.60)E-5$	$(133 \pm 1.9)E-5$	$(150 \pm 5.5)E-5$
	c	$(7.22 \pm 0.71)E-5$	$(7.10 \pm 0.75)E-5$	$(215 \pm 1.9)E-5$	$(215 \pm 7.5)E-5$
2	a	$(0.664 \pm 0.90)E-5$	$(0.245 \pm 0.95)E-5$	$(80.6 \pm 1.9)E-5$	$(30.7 \pm 13)E-5$
	b	$(2.31 \pm 0.90)E-5$	$(1.65 \pm 0.96)E-5$	$(133 \pm 1.9)E-5$	$(99.9 \pm 18)E-5$
	c	$(5.68 \pm 0.67)E-5$	$(7.07 \pm 0.70)E-5$	$(194 \pm 1.9)E-5$	$(245 \pm 7.2)E-5$
3	a	$(0.67 \pm 0.53)E-5$	$(0.562 \pm 0.56)E-5$	$(84.4 \pm 1.9)E-5$	$(71.8 \pm 8.2)E-5$
	b	$(2.24 \pm 0.57)E-5$	$(2.73 \pm 0.60)E-5$	$(133 \pm 1.9)E-5$	$(163 \pm 6.2)E-5$
	c	$(7.22 \pm 0.71)E-5$	$(7.78 \pm 0.75)E-5$	$(215 \pm 1.9)E-5$	$(235 \pm 7.8)E-5$
4	a	$(1.74 \pm 0.54)E-5$	$(2.25 \pm 0.57)E-5$	$(132 \pm 1.9)E-5$	$(171 \pm 6.8)E-5$
	b	$(2.24 \pm 0.57)E-5$	$(2.91 \pm 0.60)E-5$	$(133 \pm 1.9)E-5$	$(174 \pm 5.9)E-5$
	c	$(7.22 \pm 0.71)E-5$	$(8.26 \pm 0.75)E-5$	$(215 \pm 1.9)E-5$	$(249 \pm 7.8)E-5$

Table 2. Molar ratio comparison including precision error only.

Upon determination of the dissolved air concentration using both the direct sample method and Henry's law, the results did not agree. As can be seen in Table 2, the values obtained varied in some cases by an order of magnitude or more. Possible reasons for lack of agreement could include lack of equilibrium and lack of a dilute solution, requirements mentioned earlier for applicability of Henry's law. The system used in experimentation had flowing fluid and pressure differences at various points in the fluid loop, and thus was inherently not in equilibrium. Also mentioned earlier was the fact that ammonia in water was a solution that was not dilute enough for Henry's law to apply. Air is soluble in FC-72 up to 48% by volume at 25°C (3M, 1999), which is greater than the 31% solubility of ammonia in water. The fact that air is more soluble in FC-72 than ammonia is in water would indicate that Henry's law may not be applicable to air in FC-72. Another possible reason for the lack of agreement could involve the value used for Henry's constant. The temperatures in the current experiment fall outside the temperature bounds given previously in reference to the Henry's constant used for calculation. As a result, the value may not be valid for the current research.

Horacek et al. (2003, 2004), mentioned that while partial pressures were used to calculate the amount of dissolved air in the cooling fluid, nothing could be said about the

distribution of air throughout the flowing system at any given time. It may be appropriate to draw a similar conclusion concerning the current experiment, which could also help explain the lack of agreement between values obtained using Henry's law and those using the aire-ometer.

The proposed empirical mathematical model was evaluated through comparison of experimental data and predicted data. Experimental data from Runs 1b, 3b, and 4b, where $C_m = 10\%$, $10 \leq \Delta T_{sc} \leq 12^\circ\text{C}$, and $\dot{V} = 6.31, 8.41, \text{ and } 10.5 \text{ cm}^3/\text{s}$ (6.0, 8.0, and 10.0 gph), was used to obtain functional relationships by the method previously discussed. Equation (18), in conjunction with Equations (20) and (21) were then used to predict the behavior of surface heat flux at $\dot{V} = 7.36 \text{ and } 9.46 \text{ cm}^3/\text{s}$ (7.0 and 9.0 gph). The experimental and predicted results were plotted and compared. Figure 30 shows these results. Experimental data is depicted using isolated points, while predicted data is depicted using solid lines. As can be seen in the plot, the predicted heat flux compares well with the experimental data.

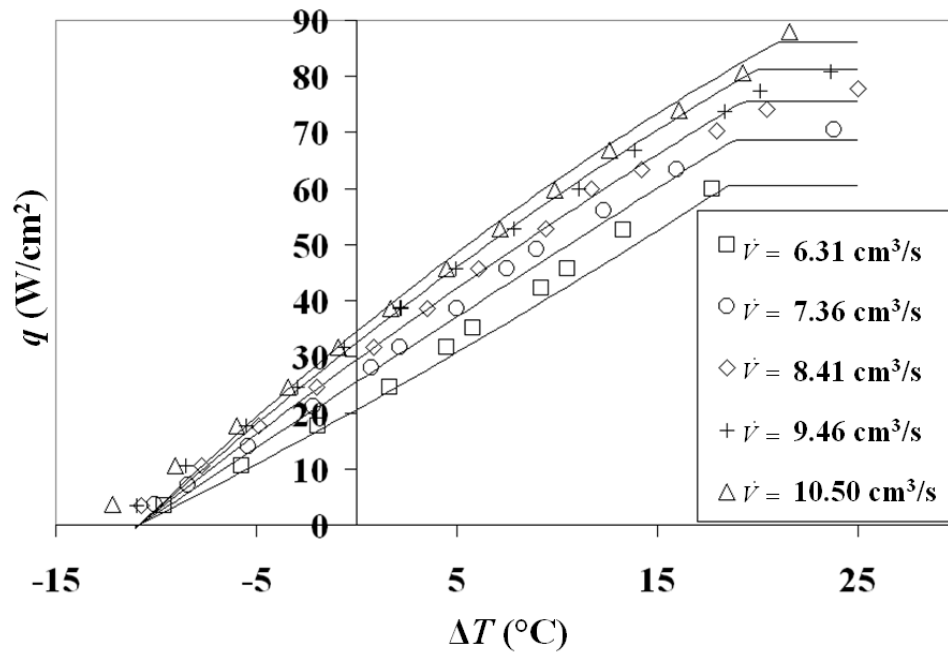


Figure 30. Mathematical fit with experimental data included.

V. Conclusions

The effect of dissolved air on the heat transfer performance of a partially-confined FC-72 spray was investigated for $5 \leq C_m \leq 18\%$. For the most part, there was no significant variation in heat transfer performance due to varying dissolved air in the spray system when the pressure, or P_{ch} , of the spray chamber was thermally controlled. It was theorized that the effect on CHF attributed by previous researchers to varying air content may have been more directly a result of varying saturation pressure as a result of varying system pressure. Further testing involving constant air content with varying pressure could provide more insight into whether this was indeed the case. If the effect on CHF observed previously was actually a more direct result of system pressure, controlling that pressure could help control CHF, regardless of the amount of air in the system. Such knowledge would be greatly useful in real-world application. Tables 3 and 4 show experimental parameters and results from current and previous research. Observation of gaps in the table, and thus in research to date, could help direct future research efforts.

When comparing dissolved air concentration measurements obtained using fluid samples and those obtained using Henry's law, the results did not agree. The applicability of Henry's law to the current system was found to be questionable due to inherent lack of equilibrium, the possibility that the concentration of air in the working fluid was too high for the solution to be considered dilute, and the use of an incorrect Henry's constant.

An empirical mathematical model correlating flow rate, subcooling, sensible heat, and critical heat flux using experimental data was also presented. The model was used to predict the behavior of two test runs and agreed well with experimental data. This may provide a useful, reduced order, empirical approach that could be used to model spray cooling components imbedded into system level thermal management models.

Current Data	Fluid	\dot{V} (cm ³ /s)	ΔT_{sc} (°C)	P_{ch} (kPa)	C_m (%)	q_{CHF}^{CHF} (W/cm ²)
	FC-72	6.35	11.40	57.78	8	65.18
		6.28	11.01	57.23	10	63.36
		6.28	11.33	72.81	18	62.83
		8.54	8.91	60.12	5	69.48
		8.50	10.40	79.78	10	69.34
		8.39	8.22	80.40	16	60.72
		8.81	11.86	40.27	5	71.64
		8.37	11.94	59.71	10	76.84
		8.42	12.18	76.60	18	76.92
		10.50	12.41	61.16	8	91.09
		10.43	12.67	61.64	10	90.64
		10.53	12.83	79.29	18	87.35
Lin and Ponnappan	Fluid	\dot{V} (cm ³ /s)	ΔT_{sc} (°C)	Nozzle Pressure Drop (kPa)	C_m (%)	q_{CHF}^{CHF} (W/cm ²)
	FC-72	1.92	minimized	103		65
		2.34	minimized	172		72.5
		2.56	minimized	241		78.5
		2.97	minimized	310		83.5
Horacek et al.	Fluid	\dot{V} (cm ³ /s)	$T_{sat} - T_{spray}$ (°C)	Reservoir Pressure (kPa)	C_m (%)	q_{CHF}^{CHF} (W/cm ²)
	FC-72	0.62	2.1	33.44	degassed	41
		0.62	25.7	33.44	degassed	47
		0.62	20.5	67.89	gaseous	52
		0.62	31.7	101.33	gaseous	56
		0.62	38.6	123.62	gaseous	64.5

Table 3. Research parameters and results.

Estes and Mudawar	Fluid	\dot{V} (cm ³ /s)	ΔT_{sc} (°C)	Pressure (kPa)	C_m (%)	q_{CHF} (W/cm ²)
	FC-72	3.53	33	103		93
		5.55	33	103		115
		7.57	33	103		136
		8.08	33	103		97
		12.20	33	103		126
		17.30	33	103		166
		12.60	33	103		109
		18.90	33	103		146
		25.20	33	103		177
Rybicki and Mudawar	Fluid	\dot{V} (cm ³ /s)	ΔT_{sc} (°C)	Pressure (kPa)	C_m (%)	q_{CHF} (W/cm ²)
	PF-5052	3.09	27	101		144
		3.54	27	101		155
		3.79	27	101		160
		9.02	27	101		177
		9.99	27	101		194
		11.1	27	101		200
		12.22	27	101		195
		18.49	27	101		210
		20.5	27	101		207
		3.54	27	101		155
		3.54	23	101		144
		9.99	27	101		184
		9.99	23	101		173
		9.99	13	101		128
		16.48	27	101		213
		16.48	23	101		196
		16.48	13	101		137

Table 4. Research parameters and results (continued).

APPENDIX A: PROCEDURES

Test Rig Fill Procedure:

- 1) Start up the spray cooling flight package and data acquisition system.
- 2) Before filling the system, the fluid in the loop must be drained and the lines must be purged.
- 3) To empty the fluid loop, connect a piece of poly-flo tubing to the drain/fill hand valve located on the bottom shelf of the rig. Place the end of the tubing not connected to the rig into a container large enough to hold at least 2 liters of fluid.
- 4) Turn on the nozzle pump and sump pump for the bottom nozzle.
- 5) Open the drain/fill hand valve located on the bottom shelf of the rig.
- 6) Allow as much of the fluid as possible to drain into the container. Toggle the valves on the control panel to ensure as much fluid has been removed as possible.
- 7) Prior to purging of the system, the valve positions on the control panel should be as follows:
 - Drain closed
 - Toggle between normal and bypassed
 - Nozzle pump open
 - Toggle between bottom and top sump valves
 - Toggle between bottom and top nozzle
- 8) Purge the system using nitrogen from a compressed gas cylinder. Use a piece of Poly-flo tubing to connect the nitrogen tank to the hand drain/fill valve located on the upper shelf of the test rig.
- 9) Ensure the drain/fill hand valve located on the bottom shelf of the rig is open, and open the valve on the compressed gas cylinder, allowing nitrogen to flow through the system and remove residual FC-72.
- 10) Using the tubing assembly specified for filling the test rig, attach a roughing vacuum pump to both of the hand drain/fill valves on the FC-72 fluid loop and to the 4-way joint connection on the spray chamber.
- 11) The valve switches on the control panel should be in the following positions:
 - Drain open
 - Toggle between top and bottom nozzle

- Top sump open
- Nozzle pump open
- Toggle between normal flow and bypass
- Bottom sump open

12) Open both hand drain/fill valves should be open.

13) Turn the roughing pump on and allow it to run until any residual fluid has been removed.

Allow it to run overnight, if necessary.

14) Close the hand valves and remove the roughing pump.

15) Connect the turbo vacuum pump in the same way the roughing pump was attached.

16) Turn the turbo pump on and allow to run until the system has reached $\sim 1 \times 10^{-3}$ Torr.

17) Prior to filling, ensure that the valve switches located on the control panel are in the following positions:

- Drain closed
- Bottom nozzle
- Top sump closed
- Nozzle pump open
- Bypass on
- Bottom sump closed

18) Open both hand drain/fill valves.

******If only topping off the rig, begin procedure here******

19) At a location suitable for boiling liquid, pour FC-72 liquid through a filter into the polycarbonate flask used for filling the test rig.

20) Place the specialized stopper into the flask, and secure it using the nuts and bolts provided.

21) Place the drain tubing leading from the Pyrex flask stopper into a small beaker large enough to hold at least 200 ml of fluid.

22) Secure the specialized stopper for the polycarbonate flask used for filling the test rig using the nuts and bolts provided.

- 23) Attach the tubing leading from the polycarbonate flask labeled “To Roughing Pump” to the roughing pump, and the tubing labeled “To Pyrex Flask” to the empty valve on the stopper of the Pyrex flask.
- 24) Ensure all bolts are tight, and place the Pyrex flask on the hot plate.
- 25) Close the valve on the Pyrex flask leading to the polycarbonate flask, and open the valve on the Pyrex flask leading to the small beaker.
- 26) Turn the roughing pump on.
- 27) Open both valves on the polycarbonate flask.
- 28) Turn the hot plate on high. As the FC-72 begins to boil, turn the heater down to low.
- 29) Allow the FC-72 to boil for three minutes, then turn off the hot plate.
- 30) Close the valve leading from the polycarbonate flask to the roughing pump and from the Pyrex flask to the small beaker.
- 31) Turn off the roughing pump.
- 32) Open the valve leading from the Pyrex flask to the polycarbonate flask.
- 33) Allow the FC-72 to siphon from the Pyrex flask into the polycarbonate flask.
- 34) Close both valves leading to the tubing connecting the Pyrex and polycarbonate flasks.
- 35) Open the valve leading from the polycarbonate flask to the small beaker, preventing a pressure build-up in the Pyrex flask.
- 36) Disconnect the tubing attached to the stopper of the polycarbonate flask from the roughing pump and wind the poly-flo up, out of the way.
- 37) Disconnect the tubing leading from the Pyrex flask to the polycarbonate flask at the valve on the stopper of the polycarbonate flask.
- 38) At the test rig, connect the section of poly-flo tubing labeled “To Flask” to the polycarbonate flask using the valve that had previously lead to the Pyrex flask in the boiling setup.
- 39) Open the valve on the tubing assembly leading from the turbo pump to the polycarbonate flask, but leave the valve on the stopper of the polycarbonate flask closed.
- 40) Close the valve leading from the pump to the tubing assembly, and invert the flask.
- 41) Open both valves on the flask, and ensure the hand drain/fill valve located on the bottom shelf is open.
- 42) Allow FC-72 to siphon into the test rig.

- 43) Once the fluid level in the flask ceases to decrease, close the valves on the flask, along with the hand drain/fill valve on the test rig.
- 44) Turn the turbo pump off.
- 45) Remove the tubing assembly.

Experimental Procedure for Aire-ometer Tests:

- 1) Start up the spray cooling flight package and data acquisition system. After letting the rig equilibrate for approximately ten minutes, take a chamber temperature and pressure reading. Record the results in the lab book. Note the date and time.
- 2) Flip the nozzle flow switch on the control panel down into bypass position. Check the pressure of pump 1 out. If this pressure is not between 15 and 20 psia, adjust the throttling valve on the test rig.
- 3) Attach the sample collection Tygon tubing assembly to the drain/fill hand valve location on the bottom shelf of the rig.
- 4) Connect the sample syringe to the three-way valve on the Tygon tubing assembly. The blue handle on the valve should be pointed in the direction of the syringe, closing that section of the assembly to flow.
- 5) Open the drain/fill hand valve on the rig. Bleed out the FC-72 that has been exposed to air (trace tubing back to Pump 1) through the Tygon drain tube and into a small accumulation beaker. Close the hand valve.
- 6) Close the Tygon drain tube portion of the assembly by pointing the blue handle on the three-way valve in the direction of the drain tube. Open the hand valve. Let 1-2 cc's of FC-72 enter the syringe, then close the hand valve. Close the portion of tubing leading to the drain/fill valve on the rig using the blue handle on the three-way valve. Expel the contents of the syringe through the Tygon drain tube and into the accumulation beaker. This should remove any remaining air located in the syringe.
- 7) Close off the drain tube by turning the blue handle on the three-way towards it. Open the drain/fill hand valve on the rig. Let the syringe fill with 4-5 cc's of FC-72, and close the hand valve. Close the portion of tubing leading to the drain/fill valve on the rig by turning the blue handle on the three-way valve in that direction. Remove the syringe from the three way valve.
- 8) Flip the nozzle flow switch on the control panel out of bypass position, to normal flow.
- 9) Insert the syringe into the three-way valve on the aire-ometer. Turn the blue handle on the three-way valve toward the unused channel.

- 10) Turn the stopcock located on the top right side of the aire-ometer so that the green dot is pointed downward. Draw a small fluid sample of approximately $\frac{1}{2}$ cc into the aire-ometer tube by turning the hand crank on the right side of the aire-ometer base in a clockwise direction. Turn the aire-ometer stopcock so that the green dot is pointing upward, and expel the fluid from the aire-ometer tube by turning the hand crank in a counter-clockwise direction until the top of the mercury in the tube reaches the bottom of the stopcock.
- 11) Turn the stopcock so that the green dot is pointed downward, and draw in a new fluid sample until the mercury is approximately $\frac{1}{2}$ " below the 1 cc calibrated mark on the aire-ometer tube.
- 12) Turn the stopcock so that the green dot is pointed upward, and bring the mercury up to the 1 cc mark. Turn the stopcock to a horizontal position.
- 13) Read the pressure gauge and note the reading for future reference.
- 14) Turn the hand crank clockwise, bringing the mercury level down to the 4 cc mark. Allow it to rest at that level for 1 minute, then turn the hand crank counter-clockwise until the pressure gauge reads the original reference pressure.
- 15) Repeat step 14 twice more.
- 16) The graduated aire-ometer tube now contains mercury at the bottom, a level of FC-72 liquid in the middle, and a level of air which was removed from the FC-72 at the top. The % air is the reading on the aire-ometer tube which separates the level of air and the level of FC-72 liquid.
- 17) Record the % air in the lab book.
- 18) Turn the stopcock so the green dot points upward, and expel the sample, bringing the mercury back up to the bottom of the stopcock.
- 19) For additional sample tests, repeat steps 11-18.
- 20) Turn the stopcock to the horizontal position, closing off the aire-ometer tube.

Membrane Filter Procedure:

- 1) Place the membrane filter on a ring stand fitted with a rubberized clasp to secure the filter.
- 2) On one side of the membrane filter is a single valve on the end of the filter. On the other side of the filter are two valves, one on the body of the filter, and the other on the end of the filter.
- 3) Attach the roughing pump to the valve on the side of the membrane with a single valve using poly-flo tubing.
- 4) Attach the valve at the opposite end of the membrane filter to the hand drain/fill valve on the bottom shelf of the test rig using poly-flo tubing.
- 5) Attach the valve on the body of the membrane filter to the hand drain/fill valve on the top shelf of the test rig using poly-flo tubing.
- 6) Start up the spray cooling flight package and data acquisition system.
- 7) Place the valve switches on the control panel to the following positions:
 - Drain closed
 - Bottom nozzle
 - Top sump closed
 - Nozzle pump open
 - Normal flow
 - Bottom sump open
- 8) Turn on Pump 1 (nozzle) and Pump 3 (scav).
- 9) Turn on the roughing pump.
- 10) Open the plug valves attached to the membrane filter.
- 11) Open the hand drain/fill valves on the test rig.
- 12) Adjust the fluid flow as necessary to ensure adequate filtering.
- 13) Monitor the chamber pressure to determine how long to allow the fluid to flow through the filter.
- 14) When finished, close all valves and turn off the roughing pump.
- 15) Disconnect the tubing from the pump and the valves on the test rig, and attach the liquid lines from the filter together, to alleviate fluid loss from the membrane filter while not being used.

APPENDIX B:

THERMOCOUPLE CALIBRATION

Thermocouple calibration was performed using an ice point calibrator (Hart Scientific Model #9101), a calibration bath (Hart Scientific Model #6330), and a precision platinum RTD (Hart Scientific Model #1502A). The calibration bath was filled with silicon oil and the temperature of the bath was controlled using a laptop and the RTD. The RTD was used to determine the temperature of the calibration bath at all times. The ice point was used as a reference temperature. Not every thermocouple on the test rig was calibrated. The calibrated thermocouples included those in the chamber, those attached to the pedestal, and those in the reheater. A Visual Basic program written by Richard Harris, of the University of Dayton Research Institute was used for calibration. The thermocouples were placed in the calibration bath, set at a specified temperature. The bath temperature was increased in increments until a maximum temperature of 120°C was reached, at which point the temperature was decreased in similar increments until the initial temperature was reached once again. At each increment, the RTD and thermocouple temperatures were recorded for 2.5 hours, allowing the bath to reach steady state at each temperature increment. Following calibration, the data was plotted as the RTD temperature versus the thermocouple temperature for each thermocouple, a linear fit was used, and associated residuals were calculated. The bias error for the temperature measured using each thermocouple was calculated using the bias error associated with the RTD probe and reader along with the error taken from the linear fit when compared to the RTD value. A sample calibration plot can be seen in Fig. 31.

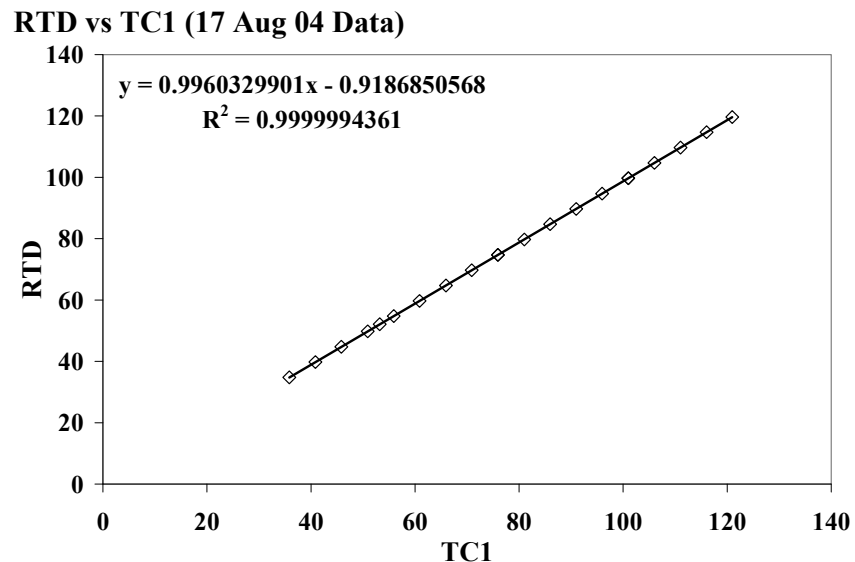


Figure 31. Sample thermocouple calibration plot.

APPENDIX C: ERROR ANALYSIS

Flow Rate (\dot{V}):

The flow rate reported for each test run was an average over the entire run. As a result, the precision error was the standard deviation of the averaged values. The bias error was the instrument error associated with the flow meter, taken from the manufacturer data. The flow meters were checked periodically to ensure the measured error fell within the manufacturer error bounds. Both types of error were added to determine the total error for the flow rate.

Amount of Subcooling (ΔT_{sc}):

The amount of subcooling for each test was defined as the difference between the heater surface temperature and the cooling fluid saturation temperature prior to activation of the heater power. The subcooling value was calculated as an average of values obtained prior to heater power activation. As a result, the precision error was the standard deviation of the averaged value. In addition to the precision error, bias error was associated with the calibration of the thermocouples used to obtain the temperature from which the subcooling was calculated. Calculation of such error can be seen below. The bias error was added to the precision error to determine the total error.

$$\Delta T_{sc} = T_s - T_{sat}$$

$$\Delta T_{sc} = f^*(T_s, T_{sat})$$

$$U_{\Delta T_{sc}} = \sqrt{\left(\frac{\partial \Delta T_{sc}}{\partial T_s} U_{T_s}\right)^2 + \left(\frac{\partial \Delta T_{sc}}{\partial T_{sat}} U_{T_{sat}}\right)^2}$$

$$\frac{\partial \Delta T_{sc}}{\partial T_s} = 1$$

$$\frac{\partial \Delta T_{sc}}{\partial T_{sat}} = -1$$

Saturation Temperature (T_{sat}):

The saturation temperature was determined as a function of chamber pressure using an equation from a lookup table in Engineering Equation Solver. The saturation temperature value was calculated as an average of values obtained over the entire test run. The precision error was the standard deviation of the averaged value. The bias error was associated with the

chamber pressure from which the saturation temperature was calculated. Calculation of such error can be seen below. The bias error was added to the precision error to determine the total error.

$$T_{sat} = -0.05661P_{ch}^2 + 3.77401P_{ch} + 13.72283$$

*Temperature was in °C and pressure was in PSIA.

$$T_{sat} = f^*(P_{ch})$$

$$U_{T_{sat}} = \sqrt{\left(\frac{\partial T_{sat}}{\partial P_{ch}} U_{P_{ch}}\right)^2}$$

$$\frac{\partial T_{sat}}{\partial P_{ch}} = -0.1132P_{ch} + 3.77401$$

Surface Temperature (T_s):

The surface temperature was determined using values obtained from multiple thermocouples in the heater pedestal, along with heater power. The precision and bias errors were both based upon the precision and bias errors associated with the thermocouple used to obtain the interface temperature. The bias error was added to the precision error to determine the total error.

$$T_s = \frac{-(1-f)}{k_{cov}A} QH_{cov} + \frac{QH_{htr}}{Ak_{htr}} \left(f - \frac{1}{2}\right) + T_{int} + \frac{fQ}{k_{sub}A} H_{sub}$$

The subcooling amount of interest was the initial subcooling, which occurred before the heater power was engaged. As a result, error associated with heater power was zero for the subcooling value of interest, along with the heater power itself. Therefore,

$$T_s = f^*(T_{int})$$

$$U_{T_s} = \sqrt{\left(\frac{\partial T_s}{\partial T_{int}} U_{T_{int}}\right)^2}$$

$$\frac{\partial T_s}{\partial T_{int}} = 1$$

The bias error associated with T_{int} was determined from the calibration of the thermocouple using an RTD, as detailed in Appendix B. The precision error for T_{int} calculated

using the standard deviation of the thermocouple values recorded before the heater power was turned on in the test run.

Chamber Pressure (P_{ch}):

The chamber pressure for each test was taken as the average chamber pressure over the entire test run. As a result, the precision error was the standard deviation of the averaged values. The pressure was measured using a transducer linked to a data acquisition system. As a result, the bias error included instrument error from the transducer itself, and digital sampling error with the data acquisition system. The calculation for bias error can be seen below. To determine the total error associated with the pressure measurement, the precision error was added to the bias error.

$$U_{P_{ch}} = U_{Transducer} + U_{Data\ Acq}$$

$$U_{Transducer} = 0.25\%FS = 0.0025 * 50PSIA = 0.13PSIA$$

$$U_{Data\ Acq} = \frac{Voltage\ Range}{2^{\#bits}} Sensitivity = \frac{5V}{2^{22}} \left(10 \frac{PSIA}{V} \right) = 1 \times 10^{-5} PSIA$$

Critical Heat Flux (q_{CHF}):

As explained previously, during testing the heater power was increased in 5 watt increments until critical heat flux was reached. Because a gap of 5 watts existed between power settings, the setting at which critical heat flux was seen to occur was not necessarily exactly the setting at which critical heat flux was actually initiated. For instance, if critical heat flux did not occur at 95 watts, but did occur at 100 watts, the power setting at which critical heat flux was triggered could have been anywhere between 95 and 100 watts. Because of this, the heater power at which critical heat flux occurred was defined to be the midpoint between the last two power settings prior to critical heat flux, with an error of ± 2.5 watts. That error was defined to be the precision error. There was also bias error associated with instrument error from the data acquisition system when measuring the voltage and resistance used to calculate the power. Total error was obtained by adding the precision error and bias error.

$$q_{CHF} = (1 - f) \left(\frac{Q}{A} \right)$$

$$q_{CHF} = f^*(Q)$$

$$U_{q_{CHF}} = \sqrt{\left(\frac{\partial q_{CHF}}{\partial Q} U_Q\right)^2}$$

$$\frac{\partial q_{CHF}}{\partial Q} = \frac{1-f}{A}$$

But,

$$Q = V_{htr} I_{htr}$$

And,

$$I_{htr} = \frac{V_{res}}{R_{res}}$$

$$\Rightarrow Q = V_{htr} \frac{V_{res}}{R_{res}}$$

$$Q = f^*(V_{htr}, V_{res}, R_{res})$$

$$U_Q = \sqrt{\left(\frac{\partial Q}{\partial V_{htr}} U_{V_{htr}}\right)^2 + \left(\frac{\partial Q}{\partial V_{res}} U_{V_{res}}\right)^2 + \left(\frac{\partial Q}{\partial R_{res}} U_{R_{res}}\right)^2}$$

$$\frac{\partial Q}{\partial V_{htr}} = \frac{V_{res}}{R_{res}}$$

$$\frac{\partial Q}{\partial V_{res}} = \frac{V_{htr}}{R_{res}}$$

$$\frac{\partial Q}{\partial R_{res}} = \frac{-V_{res} V_{htr}}{R_{res}^2}$$

The bias error associated with R_{res} was taken as 0.02% of the resistance value. The bias errors associated with V_{res} and V_{htr} were taken as 0.015% of the reading and 0.004% of the range.

Measured Air Content Percentage (C_m):

Because the divisions on the Aire-ometer were so small, the precision error was determined to be \pm one full division on the scale, which was 2%. The bias error associated with the Aire-ometer could not be found. As a result, the bias error was taken as that typically

associated with burets of similar volumes. The bias error was determined to be $\pm 1\%$. The total error was obtained by adding the precision and bias errors.

Corrected Air Content Percentage (C):

The calculation for the error associated with the corrected air content percentage can be seen below. Bias and precision error were both determined using the error associated with the values from which the corrected air content percentage was calculated. Total error was obtained by adding the bias and precision errors.

$$C = 100 \left(\frac{C^*}{1 + C^*} \right)$$

$$C = f^*(C^*)$$

$$U_C = \sqrt{\left(\frac{\partial C}{\partial C^*} U_{C^*} \right)^2}$$

$$\frac{\partial C}{\partial C^*} = \frac{100}{(1 + C^*)^2}$$

Corrected Air Volume Ratio (C*):

The calculation for the error associated with the corrected air volume ratio can be seen below. Bias and precision error were both determined using the error associated with the values from which the corrected air volume ratio was calculated. Total error was obtained by adding the bias and precision errors.

$$C^* = \frac{C_m^* P_g \left(\frac{\rho_{FC}}{\rho_{air}} \right)}{P_{g,ref} \left(\frac{\rho_{FC,ref}}{\rho_{air,ref}} \right)}$$

$$C^* = f^*(C_m^*, P_g, \rho_{FC}, \rho_{air}, P_{g,ref}, \rho_{FC,ref}, \rho_{air,ref})$$

$$U_{C^*} = \sqrt{\left(\frac{\partial C^*}{\partial C_m^*} U_{C_m^*}\right)^2 + \left(\frac{\partial C^*}{\partial P_g} U_{P_g}\right)^2 + \left(\frac{\partial C^*}{\partial \rho_{FC}} U_{\rho_{FC}}\right)^2 + \left(\frac{\partial C^*}{\rho_{air}} U_{\rho_{air}}\right)^2 + \left(\frac{\partial C^*}{\partial P_{g,ref}} U_{P_{g,ref}}\right)^2 + \left(\frac{\partial C^*}{\partial \rho_{FC,ref}} U_{\rho_{FC,ref}}\right)^2 + \left(\frac{\partial C^*}{\partial \rho_{air,ref}} U_{\rho_{air,ref}}\right)^2}$$

$$\frac{\partial C^*}{\partial C_m^*} = \frac{P_g \left(\frac{\rho_{FC}}{\rho_{air}} \right)}{\left(P_{g,ref} \right) \left(\frac{\rho_{FC,ref}}{\rho_{air,ref}} \right)}$$

$$\frac{\partial C^*}{\partial P_g} = \frac{C_m^* \left(\frac{\rho_{FC}}{\rho_{air}} \right)}{\left(P_{g,ref} \right) \left(\frac{\rho_{FC,ref}}{\rho_{air,ref}} \right)}$$

$$\frac{\partial C^*}{\partial \rho_{FC}} = \frac{C_m^* P_g \left(\frac{1}{\rho_{air}} \right)}{\left(P_{g,ref} \right) \left(\frac{\rho_{FC,ref}}{\rho_{air,ref}} \right)}$$

$$\frac{\partial C^*}{\partial \rho_{air}} = \frac{C_m^* P_g \rho_{FC}}{\left(P_{g,ref} \right) \left(\frac{\rho_{FC,ref}}{\rho_{air,ref}} \right)} \left(\frac{-1}{\rho_{air}^2} \right)$$

$$\frac{\partial C^*}{\partial P_{g,ref}} = \frac{C_m^* P_g \left(\frac{\rho_{FC}}{\rho_{air}} \right)}{\left(\frac{\rho_{FC,ref}}{\rho_{air,ref}} \right)} \left(\frac{-1}{\left(P_{g,ref} \right)^2} \right)$$

$$\frac{\partial C^*}{\partial \rho_{FC,ref}} = \frac{C_m^* P_g \left(\frac{\rho_{FC}}{\rho_{air}} \right)}{\left(P_{g,ref} \right) \left(\frac{1}{\rho_{air,ref}} \right)} \left(\frac{-1}{\left(\rho_{FC,ref} \right)^2} \right)$$

$$\frac{\partial C^*}{\partial \rho_{air,ref}} = \frac{C_m^* P_g \left(\frac{\rho_{FC}}{\rho_{air}} \right)}{\left(P_{g,ref} \right) \left(\rho_{FC,ref} \right)}$$

Measured Air Volume Ratio (C_m^*):

The calculation for the error associated with the measured air volume ratio can be seen below. Bias and precision error were both determined using the error associated with the measured air content percentage, from which the measured air volume ratio was calculated. Total error was obtained by adding the bias and precision errors.

$$C_m^* = \frac{\left(\frac{C_m}{100}\right)}{1 - \left(\frac{C_m}{100}\right)}$$

$$C_m^* = f^*(C_m)$$

$$U_{C_m^*} = \sqrt{\left(\frac{\partial C_m^*}{\partial C_m} U_{C_m}\right)^2}$$

$$\frac{\partial C_m^*}{\partial C_m} = \frac{1}{100 \left(1 - \frac{C_m}{100}\right)^2}$$

Partial Pressure (P_g):

The calculation for the error associated with the partial pressure can be seen below. Bias and precision error were both determined using the error associated with the values from which the partial pressure was calculated. Total error was obtained by adding the bias and precision errors.

$$P_g = P_{tot} - P_{sat}$$

$$P_g = f^*(P_{tot}, P_{sat})$$

$$U_{P_g} = \sqrt{\left(\frac{\partial P_g}{\partial P_{tot}} U_{P_{tot}}\right)^2 + \left(\frac{\partial P_g}{\partial P_{sat}} U_{P_{sat}}\right)^2}$$

$$\frac{\partial P_g}{\partial P_{tot}} = 1$$

$$\frac{\partial P_g}{\partial P_{sat}} = -1$$

Total Pressure (P_{tot}):

Total pressure was taken as the average chamber pressure over the test run, and was identical to P_{ch} . The precision error was taken as the standard deviation of the averaged values. The calculation for bias error can be seen below.

$$U_{P_{tot}} = U_{Transducer} + U_{Data\ Acq}$$

$$U_{Transducer} = 0.25\%FS = 0.0025 * 50PSIA = 0.13PSIA$$

$$U_{Data\ Acq} = \frac{Voltage\ Range}{2^{#bits}} Sensitivity = \frac{5V}{2^{22}} \left(10 \frac{PSIA}{V} \right) = 1 \times 10^{-5} PSIA$$

Saturation Pressure (P_{sat}):

Saturation pressure was taken as the vapor pressure corresponding to the average chamber temperature over the test run. The equation used for P_{sat} was taken from FC-72 manufacturer information, with temperature in °C, and pressure in kPa. Both bias and precision error were determined using the error associated with the chamber temperature. Total error was obtained by adding the bias and precision errors.

$$P_{sat} = \frac{\left(10^{\frac{9.729 - \frac{1562}{T_{ch} + 273}}}{1000} \right)}$$

$$P_{sat} = f^*(T_{ch})$$

$$U_{(P_{sat})} = \frac{\partial(P_{sat})}{\partial T_{ch}}$$

$$\frac{\partial P_{sat}}{\partial T_{ch}} = \left(\frac{1}{1000} \right) \left(10^{\frac{9.729 - \frac{1562}{T_{ch} + 273}}}{\ln 10} \right) \left(\frac{1562}{(T_{ch} + 273)^2} \right)$$

Chamber Temperature (T_{ch}):

The chamber temperature was determined as an average of values over the test run. The precision error for the chamber temperature was taken as the standard deviation of the averaged values. The bias error was determined from the calibration of the thermocouple using an RTD.

FC-72 Density (ρ_{FC}):

The calculation for the error associated with the FC-72 density can be seen below. The equation was taken from manufacturer information, with temperature in °C and density in kg/m³. Bias and precision error were both determined using the error associated with the values from which the density was calculated. Total error was obtained by adding the bias and precision errors.

$$\rho_{FC} = 1740 - 2.61T_{ch}$$

$$\rho_{FC} = f^*(T_{ch})$$

$$U_{\rho_{FC}} = \sqrt{\left(\frac{\partial \rho_{FC}}{\partial T_{ch}} U_{T_{ch}}\right)^2}$$

$$\frac{\partial \rho_{FC}}{\partial T_{ch}} = -2.61$$

Air Density (ρ_{air}):

Air density was calculated using a form of the ideal gas law. Bias and precision error were both determined using the error associated with the values from which the density was calculated. Total error was obtained by adding the bias and precision errors.

$$\rho_{air} = \frac{P_g}{R(T_{ch})}$$

$$\rho_{air} = f^*(P_g, T_{ch})$$

$$U_{\rho_{air}} = \sqrt{\left(\frac{\partial \rho_{air}}{\partial P_g} U_{P_g}\right)^2 + \left(\frac{\partial \rho_{air}}{\partial T_{ch}} U_{T_{ch}}\right)^2}$$

$$\frac{\partial \rho_{air}}{\partial P_g} = \frac{1}{RT_{ch}}$$

$$\frac{\partial \rho_{air}}{\partial T_{ch}} = \frac{P_g}{R} \left(\frac{-1}{T_{ch}^2} \right)$$

Reference Partial Pressure ($P_{g,ref}$):

The calculation for the error associated with the reference partial pressure can be seen below. Bias and precision error were both determined using the error associated with the values from which the partial pressure was calculated. Total error was obtained by adding the bias and precision errors.

$$P_{g,ref} = P_{tot,ref} - P_{sat,ref}$$

$$P_{g,ref} = f^*(P_{tot,ref}, P_{sat,ref})$$

$$U_{P_{g,ref}} = \sqrt{\left(\frac{\partial P_{g,ref}}{\partial P_{tot,ref}} U_{P_{tot,ref}} \right)^2 + \left(\frac{\partial P_{g,ref}}{\partial P_{sat,ref}} U_{P_{sat,ref}} \right)^2}$$

$$\frac{\partial P_{g,ref}}{\partial P_{tot,ref}} = 1$$

$$\frac{\partial P_{g,ref}}{\partial P_{sat,ref}} = -1$$

Reference Total Pressure ($P_{tot,ref}$):

Reference total pressure was taken as the chamber pressure that was hand-recorded from the data acquisition system when a fluid sample was taken for air measurement before the test run. The precision error associated with reading the value from the data acquisition system was taken as ± 0.05 PSIA. The calculation for bias error can be seen below. Total error was obtained by adding the bias and precision errors.

$$U_{(P_{tot,ref})} = U_{Transducer} + U_{Data Acq}$$

$$U_{Transducer} = 0.25\%FS = 0.0025 * 50PSIA = 0.13PSIA$$

$$U_{Data\ Acq} = \frac{Voltage\ Range}{2^{\#bits}} Sensitivity = \frac{5V}{2^{22}} \left(10 \frac{PSIA}{V} \right) = 1 \times 10^{-5} PSIA$$

Reference Saturation Pressure ($P_{sat,ref}$):

Reference saturation pressure was taken as the vapor pressure corresponding to the reference chamber temperature. The equation used for $P_{sat,ref}$ was taken from FC-72 manufacturer information, with temperature in °C, and pressure in kPa. Both bias and precision error were determined using the error associated with the chamber temperature. Total error was obtained by adding the bias and precision errors.

$$P_{sat,ref} = \frac{\left(10^{\frac{9.729 - \frac{1562}{T_{ch,ref} + 273}}}{1000} \right)}{1000}$$

$$P_{sat,ref} = f^*(T_{ch,ref})$$

$$U_{P_{sat,ref}} = \frac{\partial P_{sat,ref}}{\partial T_{ch,ref}}$$

$$\frac{\partial P_{sat,ref}}{\partial T_{ch,ref}} = \left(\frac{1}{1000} \right) \left(10^{\frac{9.729 - \frac{1562}{T_{ch,ref} + 273}}}{\ln 10} \right) \left(\frac{1562}{(T_{ch,ref} + 273)^2} \right)$$

Reference Chamber Temperature ($T_{ch,ref}$):

The reference chamber temperature was taken as the hand-recorded value from the data acquisition system when a fluid sample was taken for air measurement before the test run. The precision error associated with reading the value from the data acquisition system was taken as ± 0.05 °C. The bias error was determined from the calibration of the thermocouple using an RTD.

Reference FC-72 Density ($\rho_{FC,ref}$):

The calculation for the error associated with the reference FC-72 density can be seen below. The equation was taken from manufacturer information, with temperature in °C and density in kg/m³. Bias and precision error were both determined using the error associated with the values from which the density was calculated. Total error was obtained by adding the bias and precision errors.

$$\rho_{FC,ref} = 1740 - 2.61(T_{ch,ref})$$

$$\rho_{FC,ref} = f^*(T_{ch,ref})$$

$$U_{\rho_{FC,ref}} = \sqrt{\left(\frac{\partial \rho_{FC,ref}}{\partial T_{ch,ref}} U_{T_{ch,ref}}\right)^2}$$

$$\frac{\partial \rho_{FC,ref}}{\partial T_{ch,ref}} = -2.61$$

Reference Air Density ($\rho_{air,ref}$):

Reference air density was calculated using a form of the ideal gas law. Bias and precision error were both determined using the error associated with the values from which the density was calculated. Total error was obtained by adding the bias and precision errors.

$$\rho_{air,ref} = \frac{P_{g,ref}}{R(T_{ch,ref})}$$

$$\rho_{air,ref} = f^*(P_{g,ref}, T_{ch,ref})$$

$$U_{\rho_{air,ref}} = \sqrt{\left(\frac{\partial \rho_{air,ref}}{\partial P_{g,ref}} U_{P_{g,ref}}\right)^2 + \left(\frac{\partial \rho_{air,ref}}{\partial T_{ch,ref}} U_{T_{ch,ref}}\right)^2}$$

$$\frac{\partial \rho_{air,ref}}{\partial P_{g,ref}} = \frac{1}{R(T_{ch,ref})}$$

$$\frac{\partial \rho_{air,ref}}{\partial T_{ch,ref}} = \frac{P_{g,ref}}{R} \left(\frac{-1}{(T_{ch,ref})^2} \right)$$

Measured Molar Ratio (M_m^*) Using Henry's law:

The measured molar ratio using Henry's law was calculated using the measured partial pressure and a Henry's constant of $H(T) = 5.4 \times 10^{-5}$ mol/mol-kPa. Precision and bias errors were determined using the precision and bias errors associated with the measured partial pressure. Total error was determined by adding the precision and bias errors.

$$M_m^* = H(T)P_{g,ref}$$

$$M_m^* = f^*(P_{g,ref})$$

$$U_{M_m^*} = \sqrt{\left(\frac{\partial M_m^*}{\partial P_{g,ref}} U_{P_{g,ref}} \right)^2}$$

$$\frac{\partial M_m^*}{\partial P_{g,ref}} = H$$

Molar Ratio (M^*) Using Henry's law:

The molar ratio using Henry's law was calculated using the partial pressure and a Henry's constant of $H = 5.4 \times 10^{-5}$ mol/mol-kPa. Precision and bias errors were determined using the precision and bias errors associated with the partial pressure. Total error was determined by adding the precision and bias errors.

$$M^* = H(T)P_g$$

$$M^* = f^*(P_g)$$

$$U_{M^*} = \sqrt{\left(\frac{\partial M^*}{\partial P_g} U_{P_g} \right)^2}$$

$$\frac{\partial M^*}{\partial P_g} = H$$

Measured Molar Ratio (M_m^*) Using Measured Air Volume Ratio:

The equation used to calculate the measured molar ratio using the value for measured air volume ratio can be seen below. Precision and bias errors were determined using the precision and bias errors associated with the measured densities and air volume. Total error was determined by adding the precision and bias errors.

$$M_m^* = C_m^* \left(\frac{\rho_{air,ref}}{\rho_{FC,ref}} \right) \left(\frac{m_{FC}}{m_{air}} \right)$$
$$M_m^* = f^*(C_m^*, \rho_{air,ref}, \rho_{FC,ref})$$
$$U_{M_m^*} = \sqrt{\left(\frac{\partial M_m^*}{\partial C_m^*} U_{C_m^*} \right)^2 + \left(\frac{\partial M_m^*}{\partial \rho_{air,ref}} U_{\rho_{air,ref}} \right)^2 + \left(\frac{\partial M_m^*}{\partial \rho_{FC,ref}} U_{\rho_{FC,ref}} \right)^2}$$
$$\frac{\partial M_m^*}{\partial C_m^*} = \left(\frac{\rho_{air,ref}}{\rho_{FC,ref}} \right) \left(\frac{m_{FC}}{m_{air}} \right)$$
$$\frac{\partial M_m^*}{\partial \rho_{air,ref}} = \left(\frac{C_m^*}{\rho_{FC,ref}} \right) \left(\frac{m_{FC}}{m_{air}} \right)$$
$$\frac{\partial M_m^*}{\partial \rho_{FC,ref}} = \left(C_m^* \right) \left(\frac{m_{FC}}{m_{air}} \right) \left(-\frac{\rho_{air,ref}}{(\rho_{FC,ref})^2} \right)$$

Molar Ratio (M^*) Using Corrected Air Volume Ratio:

The equation used to calculate the measured molar ratio using the value for measured air volume ratio can be seen below. Precision and bias errors were determined using the precision and bias errors associated with the measured densities and air volume. Total error was determined by adding the precision and bias errors.

$$M^* = C^* \left(\frac{\rho_{air}}{\rho_{FC}} \right) \left(\frac{m_{FC}}{m_{air}} \right)$$
$$M^* = f^*(C^*, \rho_{air}, \rho_{FC})$$

$$U_{M^*} = \sqrt{\left(\frac{\partial M^*}{\partial C^*} U_{C^*}\right)^2 + \left(\frac{\partial M^*}{\partial \rho_{air}} U_{\rho_{air}}\right)^2 + \left(\frac{\partial M^*}{\partial \rho_{FC}} U_{\rho_{FC}}\right)^2}$$

$$\frac{\partial M^*}{\partial C^*} = \left(\frac{\rho_{air}}{\rho_{FC}}\right) \left(\frac{m_{FC}}{m_{air}}\right)$$

$$\frac{\partial M^*}{\partial \rho_{air}} = \left(\frac{C^*}{\rho_{FC}}\right) \left(\frac{m_{FC}}{m_{air}}\right)$$

$$\frac{\partial M^*}{\partial \rho_{FC}} = \left(C^*\right) \left(\frac{m_{FC}}{m_{air}}\right) \left(-\frac{\rho_{air}}{(\rho_{FC})^2}\right)$$

Values for each of the parameters used in data analysis, along with values for precision, bias, and total error can be seen on the following pages.

\dot{V}							
gph				cm ³ /s			
Value	Prec. Er.	Bias Er.	Tot. Er.	Value	Prec. Er.	Bias Er.	Tot. Er.
6.04	0.07	0.24	0.31	6.35	0.07	0.25	0.33
5.97	0.06	0.24	0.30	6.28	0.06	0.25	0.32
5.97	0.05	0.24	0.29	6.28	0.05	0.25	0.30
8.12	0.12	0.24	0.36	8.54	0.13	0.25	0.38
8.08	0.09	0.24	0.33	8.50	0.09	0.25	0.35
7.98	0.23	0.24	0.47	8.39	0.24	0.25	0.49
8.38	0.14	0.24	0.38	8.81	0.15	0.25	0.40
7.96	0.15	0.24	0.39	8.37	0.16	0.25	0.41
8.01	0.09	0.24	0.33	8.42	0.09	0.25	0.35
9.99	0.06	0.24	0.30	10.50	0.06	0.25	0.32
9.92	0.55	0.24	0.79	10.43	0.58	0.25	0.83
10.01	0.06	0.24	0.30	10.53	0.06	0.25	0.32

Table 5. FC-72 volumetric flow rate, with error.

ΔT_{sc}							
°C				K			
Value	Prec. Er.	Bias Er.	Tot. Er.	Value	Prec. Er.	Bias Er.	Tot. Er.
11.40	0.40	0.36	0.76	284.40	0.40	0.36	0.76
11.01	0.40	0.36	0.76	284.01	0.40	0.36	0.76
11.33	0.40	0.33	0.73	284.33	0.40	0.33	0.73
8.91	0.90	0.35	1.25	281.91	0.90	0.35	1.25
10.40	0.80	0.31	1.11	283.40	0.80	0.31	1.11
8.22	0.40	0.31	0.71	281.22	0.40	0.31	0.71
11.86	0.60	0.39	0.99	284.86	0.60	0.39	0.99
11.94	0.50	0.35	0.85	284.94	0.50	0.35	0.85
12.18	0.40	0.32	0.72	285.18	0.40	0.32	0.72
12.41	0.50	0.35	0.85	285.41	0.50	0.35	0.85
12.67	0.40	0.35	0.75	285.67	0.40	0.35	0.75
12.83	0.40	0.31	0.72	285.83	0.40	0.31	0.72

Table 6. Subcooled temperature, with error.

T_{sat}								
°C					K			
Value	$\partial T_{\text{sc}}/\partial T_{\text{sat}}$	Prec. Er.	Bias Er.	Tot. Er.	Value	Prec. Er.	Bias Er.	Tot. Er.
41.40	-1.00	0.40	0.35	0.75	314.40	0.40	0.35	0.75
41.20	-1.00	0.40	0.35	0.75	314.20	0.40	0.35	0.75
47.30	-1.00	0.40	0.32	0.72	320.30	0.40	0.32	0.72
42.30	-1.00	0.90	0.35	1.25	315.30	0.90	0.35	1.25
49.80	-1.00	0.80	0.31	1.11	322.80	0.80	0.31	1.11
50.00	-1.00	0.40	0.31	0.71	323.00	0.40	0.31	0.71
33.80	-1.00	0.60	0.39	0.99	306.80	0.60	0.39	0.99
42.20	-1.00	0.50	0.35	0.85	315.20	0.50	0.35	0.85
48.70	-1.00	0.40	0.31	0.71	321.70	0.40	0.31	0.71
42.70	-1.00	0.50	0.35	0.85	315.70	0.50	0.35	0.85
42.90	-1.00	0.40	0.35	0.75	315.90	0.40	0.35	0.75
49.60	-1.00	0.40	0.31	0.71	322.60	0.40	0.31	0.71

Table 7. Saturation temperature corresponding to chamber pressure, with error.

T_{int}				T_s			
$^{\circ}\text{C}$				$^{\circ}\text{C}$			
$\partial T_s / \partial T_{\text{int}}$	Prec. Er.	Bias Er.	Tot. Er.	$\partial T_{\text{sc}} / \partial T_s$	Prec. Er.	Bias Er.	Tot. Er.
1.00	0.02	0.06	0.08	1.00	0.02	0.06	0.08
1.00	0.02	0.06	0.08	1.00	0.02	0.06	0.08
1.00	0.06	0.06	0.12	1.00	0.06	0.06	0.12
1.00	0.03	0.06	0.09	1.00	0.03	0.06	0.09
1.00	0.04	0.06	0.10	1.00	0.04	0.06	0.10
1.00	0.04	0.06	0.10	1.00	0.04	0.06	0.10
1.00	0.02	0.06	0.08	1.00	0.02	0.06	0.08
1.00	0.02	0.06	0.08	1.00	0.02	0.06	0.08
1.00	0.06	0.06	0.12	1.00	0.06	0.06	0.12
1.00	0.02	0.06	0.08	1.00	0.02	0.06	0.08
1.00	0.02	0.06	0.08	1.00	0.02	0.06	0.08
1.00	0.06	0.06	0.12	1.00	0.06	0.06	0.12

Table 8. Interface and surface heater temperatures, with error.

P_{ch}							
PSIA				kPa			
Value	Prec. Er.	Bias Er.	Tot. Er.	Value	Prec. Er.	Bias Er.	Tot. Er.
8.38	0.14	0.13	0.27	57.78	0.97	0.86	1.83
8.30	0.14	0.13	0.27	57.23	0.97	0.86	1.83
10.56	0.15	0.13	0.28	72.81	1.03	0.86	1.90
8.72	0.31	0.13	0.44	60.12	2.14	0.86	3.00
11.57	0.31	0.13	0.44	79.78	2.14	0.86	3.00
11.66	0.17	0.13	0.30	80.40	1.17	0.86	2.03
5.84	0.19	0.13	0.32	40.27	1.31	0.86	2.17
8.66	0.17	0.13	0.30	59.71	1.17	0.86	2.03
11.11	0.16	0.13	0.29	76.60	1.10	0.86	1.97
8.87	0.17	0.13	0.30	61.16	1.17	0.86	2.03
8.94	0.15	0.13	0.28	61.64	1.03	0.86	1.90
11.50	0.17	0.13	0.30	79.29	1.17	0.86	2.03

Table 9. Average chamber pressure, with error.

q_{CHF}				Q		
W/cm^2				W		
Value	Prec. Er.	Bias Er.	Tot. Er.	Value	$\partial q_{CHF}/\partial Q$	Bias Er.
65.18	1.79	2.08	3.87	92.64	0.70	2.96
63.36	1.79	2.03	3.81	90.06	0.70	2.88
62.83	1.79	2.04	3.82	90.27	0.70	2.89
69.48	1.79	2.24	4.03	99.77	0.70	3.18
69.34	1.79	2.23	4.02	99.57	0.70	3.17
60.72	1.79	1.98	3.76	87.51	0.70	2.81
71.64	1.79	2.31	4.09	102.79	0.70	3.28
76.84	1.79	2.46	4.24	110.07	0.70	3.49
76.92	1.79	2.47	4.25	110.45	0.70	3.51
91.09	1.79	2.88	4.67	130.02	0.70	4.10
90.64	1.79	2.88	4.66	129.68	0.70	4.09
87.35	1.79	2.77	4.56	124.80	0.70	3.94

Table 10. Critical heat flux and heater power, with error.

V_{htr}			V_{res}			R_{res}		
V			V			Ohms		
Value	$\partial Q/\partial V_{\text{htr}}$	Bias Er.	Value	$\partial Q/\partial V_{\text{res}}$	Bias Er.	Value	$\partial Q/\partial R_{\text{res}}$	Bias Er.
34.42	269.00	0.01	26.90	344.20	0.00	0.10	-92589.80	0.00
33.96	265.00	0.01	26.50	339.60	0.00	0.10	-89994.00	0.00
33.96	266.00	0.01	26.60	339.60	0.00	0.10	-90333.60	0.00
35.67	280.00	0.01	28.00	356.70	0.01	0.10	-99876.00	0.00
35.56	280.00	0.01	28.00	355.60	0.01	0.10	-99568.00	0.00
33.30	263.00	0.01	26.30	333.00	0.00	0.10	-87579.00	0.00
36.38	283.00	0.01	28.30	363.80	0.01	0.10	-102955.40	0.00
37.43	294.00	0.01	29.40	374.30	0.01	0.10	-110044.20	0.00
37.57	294.00	0.01	29.40	375.70	0.01	0.10	-110455.80	0.00
41.00	317.00	0.01	31.70	410.00	0.01	0.10	-129970.00	0.00
40.62	319.00	0.01	31.90	406.20	0.01	0.10	-129577.80	0.00
39.85	313.00	0.01	31.30	398.50	0.01	0.10	-124730.50	0.00

Table 11. Heater and resistor voltages and resistance, with error.

C_m					C_m^*				
%									
Value	$\partial C_m^* / \partial C_m$	Prec. Er.	Bias Er.	Tot. Er.	Value	$\partial C^* / \partial C_m^*$	Prec. Er.	Bias Er.	Tot. Er.
8.00	0.01	2.00	1.00	3.00	0.09	0.97	0.02	0.01	0.04
10.00	0.01	2.00	1.00	3.00	0.11	1.06	0.02	0.01	0.04
18.00	0.01	2.00	1.00	3.00	0.22	0.93	0.03	0.01	0.04
5.00	0.01	2.00	1.00	3.00	0.05	0.27	0.02	0.01	0.03
10.00	0.01	2.00	1.00	3.00	0.11	0.52	0.02	0.01	0.04
16.00	0.01	2.00	1.00	3.00	0.19	1.00	0.03	0.01	0.04
5.00	0.01	2.00	1.00	3.00	0.05	0.89	0.02	0.01	0.03
10.00	0.01	2.00	1.00	3.00	0.11	1.11	0.02	0.01	0.04
18.00	0.01	2.00	1.00	3.00	0.22	0.97	0.03	0.01	0.04
8.00	0.01	2.00	1.00	3.00	0.09	1.11	0.02	0.01	0.04
10.00	0.01	2.00	1.00	3.00	0.11	1.14	0.02	0.01	0.04
18.00	0.01	2.00	1.00	3.00	0.22	0.99	0.03	0.01	0.04

Table 12. Measured air content by volume and measured air volume ratio, with error.

C^*					C			
Value	$\partial C / \partial C^*$	Prec. Er.	Bias Er.	Tot. Er.	Value	Prec. Er.	Bias Er.	Tot. Er.
0.08	85.06	0.02	0.01	0.04	7.77	1.97	1.09	3.06
0.12	79.98	0.03	0.01	0.04	10.57	2.17	1.06	3.23
0.20	68.99	0.03	0.02	0.04	16.94	2.01	1.08	3.09
0.01	97.18	0.01	0.01	0.02	1.42	0.85	1.27	2.12
0.06	89.29	0.02	0.01	0.03	5.51	1.52	1.28	2.80
0.19	70.57	0.03	0.02	0.04	16.00	2.08	1.06	3.14
0.05	91.26	0.02	0.01	0.03	4.47	1.89	1.10	2.99
0.12	79.21	0.03	0.01	0.04	11.00	2.25	1.05	3.30
0.21	68.04	0.03	0.02	0.05	17.52	2.06	1.06	3.12
0.10	83.13	0.03	0.01	0.04	8.83	2.24	1.06	3.30
0.13	78.70	0.03	0.01	0.04	11.28	2.29	1.04	3.33
0.22	67.46	0.03	0.02	0.05	17.87	2.09	1.05	3.14

Table 13. Corrected air volume ratio and corrected air content by volume, with error.

M_m^* from C_m^*						
Value	$\partial M^*/\partial C^*$	$\partial M^*/\partial \rho_{\text{air},m}$	$\partial M^*/\partial \rho_{\text{FC},m}$	Prec. Er.	Bias Er.	Tot. Er.
3.66E-05	4.35E-04	5.83E-04	-2.17E-08	1.01E-05	5.60E-06	1.57E-05
5.24E-05	4.43E-04	8.22E-04	-3.12E-08	1.18E-05	5.80E-06	1.76E-05
1.13E-04	5.52E-04	1.42E-03	-6.70E-08	1.27E-05	6.81E-06	1.95E-05
4.94E-06	3.43E-04	9.99E-05	-2.93E-09	3.84E-06	5.71E-06	9.55E-06
2.58E-05	4.43E-04	4.06E-04	-1.54E-08	7.43E-06	6.27E-06	1.37E-05
9.83E-05	5.16E-04	1.32E-03	-5.84E-08	1.29E-05	6.56E-06	1.94E-05
1.62E-05	3.47E-04	3.24E-04	-9.64E-09	9.01E-06	5.30E-06	1.43E-05
5.48E-05	4.43E-04	8.60E-04	-3.26E-08	1.23E-05	5.80E-06	1.81E-05
1.17E-04	5.52E-04	1.47E-03	-6.97E-08	1.32E-05	6.81E-06	2.00E-05
4.15E-05	4.29E-04	6.72E-04	-2.47E-08	1.17E-05	5.60E-06	1.73E-05
5.64E-05	4.43E-04	8.85E-04	-3.36E-08	1.27E-05	5.80E-06	1.85E-05
1.20E-04	5.52E-04	1.51E-03	-7.14E-08	1.35E-05	6.81E-06	2.03E-05

Table 14. Measured molar ratio from measured air volume ratio, with error.

M^* from C^*						
Value	$\partial M^*/\partial C^*$	$\partial M^*/\partial \rho_{\text{air}}$	$\partial M^*/\partial \rho_{\text{FC}}$	Prec. Er.	Bias Er.	Tot. Er.
3.98E-05	4.72E-04	5.86E-04	-2.37E-08	1.10E-05	6.07E-06	1.70E-05
5.52E-05	4.67E-04	8.22E-04	-3.29E-08	1.28E-05	6.29E-06	1.91E-05
1.21E-04	5.93E-04	1.43E-03	-7.24E-08	1.38E-05	7.39E-06	2.12E-05
6.88E-06	4.77E-04	1.03E-04	-4.20E-09	4.36E-06	6.19E-06	1.05E-05
3.69E-05	6.32E-04	4.18E-04	-2.26E-08	8.16E-06	6.80E-06	1.50E-05
1.24E-04	6.51E-04	1.33E-03	-7.44E-08	1.40E-05	7.12E-06	2.11E-05
1.55E-05	3.32E-04	3.25E-04	-9.23E-09	9.81E-06	5.74E-06	1.55E-05
6.03E-05	4.88E-04	8.60E-04	-3.60E-08	1.34E-05	6.29E-06	1.97E-05
1.32E-04	6.24E-04	1.48E-03	-7.93E-08	1.43E-05	7.39E-06	2.17E-05
4.82E-05	4.98E-04	6.73E-04	-2.88E-08	1.27E-05	6.07E-06	1.88E-05
6.40E-05	5.03E-04	8.85E-04	-3.82E-08	1.37E-05	6.29E-06	2.00E-05
1.40E-04	6.44E-04	1.52E-03	-8.40E-08	1.47E-05	7.39E-06	2.21E-05

Table 15. Molar ratio from corrected air volume ratio, with error.

$P_{\text{tot,ref}}$								
PSIA					kPa			
Value	$\partial P_{\text{g,ref}}/\partial P_{\text{tot,ref}}$	Prec. Er.	Bias Er.	Tot. Er.	Value	Prec. Er.	Bias Er.	Tot. Er.
7.69	1.00	0.05	0.13	0.18	53.01	0.34	0.86	1.21
7.88	1.00	0.05	0.13	0.18	54.32	0.34	0.86	1.21
9.79	1.00	0.05	0.13	0.18	67.48	0.34	0.86	1.21
6.07	1.00	0.05	0.13	0.18	41.84	0.34	0.86	1.21
7.88	1.00	0.05	0.13	0.18	54.32	0.34	0.86	1.21
9.14	1.00	0.05	0.13	0.18	63.00	0.34	0.86	1.21
6.14	1.00	0.05	0.13	0.18	42.32	0.34	0.86	1.21
7.88	1.00	0.05	0.13	0.18	54.32	0.34	0.86	1.21
9.79	1.00	0.05	0.13	0.18	67.48	0.34	0.86	1.21
7.61	1.00	0.05	0.13	0.18	52.45	0.34	0.86	1.21
7.88	1.00	0.05	0.13	0.18	54.32	0.34	0.86	1.21
9.79	1.00	0.05	0.13	0.18	67.48	0.34	0.86	1.21

Table 16. Reference total pressure, with error.

$P_{\text{sat,ref}}$								
PSIA					kPa			
Value	$\partial P_{\text{g,ref}}/\partial P_{\text{sat,ref}}$	Prec. Er.	Bias Er.	Tot. Er.	Value	Prec. Er.	Bias Er.	Tot. Er.
3.78	-1.00	0.00	0.07	0.07	26.06	0.02	0.49	0.52
4.29	-1.00	0.00	0.07	0.07	29.60	0.02	0.49	0.52
4.01	-1.00	0.00	0.07	0.07	27.61	0.02	0.49	0.52
3.90	-1.00	0.00	0.07	0.07	26.91	0.02	0.49	0.52
4.29	-1.00	0.00	0.07	0.07	29.60	0.02	0.49	0.52
3.92	-1.00	0.00	0.07	0.07	27.04	0.02	0.49	0.52
3.87	-1.00	0.00	0.07	0.07	26.70	0.02	0.49	0.52
4.29	-1.00	0.00	0.07	0.07	29.60	0.02	0.49	0.52
4.01	-1.00	0.00	0.07	0.07	27.61	0.02	0.49	0.52
4.07	-1.00	0.00	0.07	0.07	28.03	0.02	0.49	0.52
4.29	-1.00	0.00	0.07	0.07	29.60	0.02	0.49	0.52
4.01	-1.00	0.00	0.07	0.07	27.61	0.02	0.49	0.52

Table 17. Reference saturation pressure, with error.

$T_{\text{ch,ref}}$						
°C						
Value	$\partial p_{\text{FC,ref}}/\partial T_{\text{ch,ref}}$	$\partial p_{\text{air,ref}}/\partial T_{\text{ch,ref}}$	$\partial P_{\text{sat,ref}}/\partial T_{\text{ch,ref}}$	Prec. Er.	Bias Er.	Tot. Er.
20.99	-2.61	0.00	0.49	0.05	1.00	1.05
24.09	-2.61	0.00	0.49	0.05	1.00	1.05
22.39	-2.61	0.00	0.49	0.05	1.00	1.05
21.77	-2.61	0.00	0.49	0.05	1.00	1.05
24.09	-2.61	0.00	0.49	0.05	1.00	1.05
21.88	-2.61	0.00	0.49	0.05	1.00	1.05
21.58	-2.61	0.00	0.49	0.05	1.00	1.05
24.09	-2.61	0.00	0.49	0.05	1.00	1.05
22.39	-2.61	0.00	0.49	0.05	1.00	1.05
22.76	-2.61	0.00	0.49	0.05	1.00	1.05
24.09	-2.61	0.00	0.49	0.05	1.00	1.05
22.39	-2.61	0.00	0.49	0.05	1.00	1.05

Table 18. Reference chamber temperature, with error.

$P_{g,ref}$									
PSIA					kPa				
Value	$\partial C^*/\partial P_{g,ref}$	Prec. Er.	Bias Er.	Tot. Er.	Value	$\partial \rho_{air,ref}/\partial P_{g,ref}$	Prec. Er.	Bias Er.	Tot. Er.
3.91	-0.02	0.05	0.14	0.13	26.95	0.00	0.35	0.99	1.34
3.59	-0.03	0.05	0.14	0.13	24.71	0.00	0.35	0.99	1.34
5.78	-0.04	0.05	0.14	0.13	39.87	0.00	0.35	0.99	1.34
2.17	-0.03	0.05	0.14	0.13	14.93	0.00	0.35	0.99	1.34
3.59	-0.03	0.05	0.14	0.13	24.71	0.00	0.35	0.99	1.34
5.22	-0.04	0.05	0.14	0.13	35.97	0.00	0.35	0.99	1.34
2.27	-0.02	0.05	0.14	0.13	15.62	0.00	0.35	0.99	1.34
3.59	-0.03	0.05	0.14	0.13	24.71	0.00	0.35	0.99	1.34
5.78	-0.04	0.05	0.14	0.13	39.87	0.00	0.35	0.99	1.34
3.54	-0.02	0.05	0.14	0.13	24.42	0.00	0.35	0.99	1.34
3.59	-0.03	0.05	0.14	0.13	24.71	0.00	0.35	0.99	1.34
5.78	-0.04	0.05	0.14	0.13	39.87	0.00	0.35	0.99	1.34

Table 19. Reference partial pressure, with error.

$\rho_{\text{FC,ref}}$					$\rho_{\text{air,ref}}$				
kg/m^3					kg/m^3				
Value	$\partial C^*/\partial \rho_{\text{FC,ref}}$	Prec. Er.	Bias Er.	Tot. Er.	Value	$\partial C^*/\partial \rho_{\text{air,ref}}$	Prec. Er.	Bias Er.	Tot. Er.
1685.22	0.00	0.13	2.61	2.74	0.03	2.74	0.00	0.00	0.00
1677.13	0.00	0.13	2.61	2.74	0.03	3.83	0.00	0.00	0.00
1681.56	0.00	0.13	2.61	2.74	0.05	4.71	0.00	0.00	0.00
1683.18	0.00	0.13	2.61	2.74	0.02	3.08	0.00	0.00	0.00
1677.13	0.00	0.13	2.61	2.74	0.03	3.96	0.00	0.00	0.00
1682.89	0.00	0.13	2.61	2.74	0.04	4.53	0.00	0.00	0.00
1683.68	0.00	0.13	2.61	2.74	0.02	2.85	0.00	0.00	0.00
1677.13	0.00	0.13	2.61	2.74	0.03	3.83	0.00	0.00	0.00
1681.56	0.00	0.13	2.61	2.74	0.05	4.71	0.00	0.00	0.00
1680.60	0.00	0.13	2.61	2.74	0.03	3.03	0.00	0.00	0.00
1677.13	0.00	0.13	2.61	2.74	0.03	3.83	0.00	0.00	0.00
1681.56	0.00	0.13	2.61	2.74	0.05	4.71	0.00	0.00	0.00

Table 20. Reference FC-72 and air densities, with error.

M^*_m from Henry's law				M^* from Henry's law			
Value	Prec. Er.	Bias Er.	Tot. Er.	Value	Prec. Er.	Bias Er.	Tot. Er.
1.46E-03	1.87E-05	5.36E-05	7.22E-05	1.53E-03	5.71E-05	7.99E-05	1.37E-04
1.33E-03	1.87E-05	5.36E-05	7.22E-05	1.50E-03	5.52E-05	8.00E-05	1.35E-04
2.15E-03	1.87E-05	5.36E-05	7.22E-05	2.15E-03	7.48E-05	8.56E-05	1.60E-04
8.06E-04	1.87E-05	5.36E-05	7.22E-05	3.07E-04	1.32E-04	1.18E-04	2.49E-04
1.33E-03	1.87E-05	5.36E-05	7.22E-05	9.99E-04	1.84E-04	1.28E-04	3.12E-04
1.94E-03	1.87E-05	5.36E-05	7.22E-05	2.45E-03	7.17E-05	8.83E-05	1.60E-04
8.44E-04	1.87E-05	5.36E-05	7.22E-05	7.18E-04	8.21E-05	7.65E-05	1.59E-04
1.33E-03	1.87E-05	5.36E-05	7.22E-05	1.63E-03	6.23E-05	8.00E-05	1.42E-04
2.15E-03	1.87E-05	5.36E-05	7.22E-05	2.35E-03	7.78E-05	8.56E-05	1.63E-04
1.32E-03	1.87E-05	5.36E-05	7.22E-05	1.71E-03	6.75E-05	7.99E-05	1.47E-04
1.33E-03	1.87E-05	5.36E-05	7.22E-05	1.74E-03	5.87E-05	8.00E-05	1.39E-04
2.15E-03	1.87E-05	5.36E-05	7.22E-05	2.49E-03	8.09E-05	8.56E-05	1.66E-04

Table 21. Molar ratios calculated using Henry's law, with error.

P_{tot}								
PSIA					kPa			
Value	$\partial P_g / \partial P_{\text{tot}}$	Prec. Er.	Bias Er.	Tot. Er.	Value	Prec. Er.	Bias Er.	Tot. Er.
8.38	1.00	0.14	0.13	0.27	57.76	0.97	0.86	1.83
8.30	1.00	0.14	0.13	0.27	57.21	0.97	0.86	1.83
10.56	1.00	0.15	0.13	0.28	72.79	1.03	0.86	1.90
8.72	1.00	0.31	0.13	0.44	60.11	2.14	0.86	3.00
11.57	1.00	0.31	0.13	0.44	79.75	2.14	0.86	3.00
11.66	1.00	0.17	0.13	0.30	80.37	1.17	0.86	2.03
5.84	1.00	0.19	0.13	0.32	40.25	1.31	0.86	2.17
8.66	1.00	0.17	0.13	0.30	59.69	1.17	0.86	2.03
11.11	1.00	0.16	0.13	0.29	76.58	1.10	0.86	1.96
8.87	1.00	0.17	0.13	0.30	61.14	1.17	0.86	2.03
8.94	1.00	0.15	0.13	0.28	61.62	1.03	0.86	1.90
11.50	1.00	0.17	0.13	0.30	79.27	1.17	0.86	2.03

Table 22. Total pressure, with error.

P_{sat}								
PSIA					kPa			
Value	$\partial P_g / \partial P_{\text{sat}}$	Prec. Er.	Bias Er.	Tot. Er.	Value	Prec. Er.	Bias Er.	Tot. Er.
4.28	-1.00	0.06	0.17	0.24	29.49	0.43	1.20	1.64
4.29	-1.00	0.05	0.17	0.22	29.55	0.34	1.20	1.54
4.83	-1.00	0.12	0.19	0.31	33.29	0.84	1.33	2.17
7.89	-1.00	0.17	0.29	0.46	54.41	1.18	2.00	3.18
8.93	-1.00	0.39	0.32	0.71	61.53	2.70	2.21	4.91
5.09	-1.00	0.07	0.20	0.27	35.06	0.47	1.39	1.86
3.95	-1.00	0.09	0.16	0.26	27.24	0.64	1.13	1.77
4.29	-1.00	0.05	0.17	0.22	29.55	0.34	1.20	1.54
4.83	-1.00	0.12	0.19	0.31	33.29	0.84	1.33	2.17
4.28	-1.00	0.06	0.17	0.24	29.49	0.43	1.20	1.64
4.29	-1.00	0.05	0.17	0.22	29.55	0.34	1.20	1.54
4.83	-1.00	0.12	0.19	0.31	33.29	0.84	1.33	2.17

Table 23. Saturation pressure, with error.

T_{ch}						
°C						
Value	$\partial\rho_{\text{FC}}/\partial T_{\text{ch}}$	$\partial\rho_{\text{air}}/\partial T_{\text{ch}}$	$\partial P_{\text{sat}}/\partial T_{\text{ch}}$	Prec. Er.	Bias Er.	Tot. Er.
24.00	-2.61	0.00	1.20	0.36	1.00	1.36
24.05	-2.61	0.00	1.20	0.28	1.00	1.28
27.00	-2.61	0.00	1.33	0.63	1.00	1.63
39.82	-2.61	0.00	2.00	0.59	1.00	1.59
43.20	-2.61	0.00	2.21	1.22	1.00	2.22
28.30	-2.61	0.00	1.39	0.34	1.00	1.34
22.06	-2.61	0.00	1.13	0.57	1.00	1.57
24.05	-2.61	0.00	1.20	0.28	1.00	1.28
27.00	-2.61	0.00	1.33	0.63	1.00	1.63
24.00	-2.61	0.00	1.20	0.36	1.00	1.36
24.05	-2.61	0.00	1.20	0.28	1.00	1.28
27.00	-2.61	0.00	1.33	0.63	1.00	1.63

Table 24. Chamber temperature, with error.

P_g									
PSIA					kPa				
Value	$\partial C^*/\partial P_g$	Prec. Er.	Bias Er.	Tot. Er.	Value	$\partial \rho_{air}/\partial P_g$	Prec. Er.	Bias Er.	Tot. Er.
4.10	0.02	0.15	0.21	0.37	28.27	0.00	1.06	1.48	2.54
4.01	0.03	0.15	0.21	0.36	27.66	0.00	1.02	1.48	2.50
5.73	0.04	0.19	0.23	0.42	39.50	0.00	1.33	1.59	2.92
0.83	0.07	0.35	0.32	0.67	5.69	0.00	2.44	2.18	4.62
2.64	0.04	0.50	0.34	0.84	18.22	0.00	3.44	2.38	5.82
6.57	0.03	0.18	0.24	0.42	45.31	0.00	1.26	1.63	2.90
1.89	0.03	0.21	0.21	0.42	13.02	0.00	1.46	1.42	2.88
4.37	0.03	0.18	0.21	0.39	30.14	0.00	1.22	1.48	2.70
6.28	0.04	0.20	0.23	0.43	43.29	0.00	1.39	1.59	2.97
4.59	0.02	0.18	0.21	0.40	31.65	0.00	1.25	1.48	2.73
4.65	0.02	0.16	0.21	0.37	32.07	0.00	1.09	1.48	2.57
6.67	0.03	0.21	0.23	0.44	45.98	0.00	1.44	1.59	3.03

Table 25. Partial pressure, with error.

ρ_{FC}					ρ_{air}				
kg/m^3					kg/m^3				
Value	$\partial C^*/\partial \rho_{FC}$	Prec. Er.	Bias Er.	Tot. Er.	Value	$\partial C^*/\partial \rho_{air}$	Prec. Er.	Bias Er.	Tot. Er.
1677.36	0.00	0.94	2.61	3.55	0.03	-2.64	0.00	0.00	0.00
1677.23	0.00	0.73	2.61	3.34	0.03	-3.43	0.00	0.00	0.00
1669.53	0.00	1.64	2.61	4.25	0.05	-4.83	0.00	0.00	0.00
1636.07	0.00	1.54	2.61	4.15	0.01	-8.57	0.00	0.00	0.01
1627.25	0.00	3.18	2.61	5.79	0.02	-5.72	0.00	0.00	0.01
1666.14	0.00	0.89	2.61	3.50	0.05	-3.68	0.00	0.00	0.00
1682.42	0.00	1.49	2.61	4.10	0.02	-3.43	0.00	0.00	0.00
1677.23	0.00	0.73	2.61	3.34	0.04	-3.14	0.00	0.00	0.00
1669.53	0.00	1.64	2.61	4.25	0.05	-4.40	0.00	0.00	0.00
1677.36	0.00	0.94	2.61	3.55	0.04	-2.35	0.00	0.00	0.00
1677.23	0.00	0.73	2.61	3.34	0.04	-2.95	0.00	0.00	0.00
1669.53	0.00	1.64	2.61	4.25	0.05	-4.15	0.00	0.00	0.00

Table 26. FC-72 and air densities, with error.

References

- 3M Specialty Materials, “Fluorinert™ Electronic Liquids for Electronic Reliability Testing,” Company Data Sheet, 1999, p. 3.
- 3M Specialty Materials, “Fluorinert™ Electronic Liquid FC-72 Product Information,” Company Data Sheet, 2000, p.2.
- Baysinger, K. M., Yerkes, K. L., Michalak, T. E., Harris, R. J., and McQuillen, J., “Design of a Microgravity Spray Cooling Experiment,” *Proc. 42nd AIAA Aerospace Sciences Conference and Exhibit*, Paper No. AIAA-2004-0966, 2004.
- Baysinger, K. M., Yerkes, K. L., and Thomas, S. K., “Experimental Testing and Numerical Modeling of Spray Cooling Under Terrestrial Gravity Conditions,” AFRL-PR-WP-TR-2005-2047, 2005.
- Baysinger, K. M., “Experimental Testing and Numerical Modeling of Spray Cooling Under Terrestrial Gravity Conditions,” Masters Thesis, Wright State University, Department of Mechanical and Materials Engineering, 2005.
- Celata, G. P., Cumo, M., and Mariani, A., “Burnout in Highly Subcooled Water Flow Boiling in Small Diameter Tubes,” *Int. J. Heat Mass Transfer*, Vol. 36, No. 5, 1993, pp. 1269-1285.
- Çengel, Y. A. and M. A. Boles, Thermodynamics: An Engineering Approach, 4th ed. New York: The McGraw-Hill Companies, Inc., 1989, pp. 761-762.
- Committee on Spacecraft Exposure Guidelines, Committee on Toxicology, National Research Council, and National Academy of Sciences, Spacecraft Water Exposure Guidelines for Selected Contaminants: Volume 2. Washington DC: The National Academy of Sciences, 2007, p. 39.
- Dawson, H. and diMarzo, M., “Multi-Droplet Evaporative Cooling: Experimental Results,” *AIChE Symposium Series*, Vol. 89, No. 295, 1993, pp. 122-131.
- Estes, K. A. and Mudawar, I., “Comparison of Two-Phase Electronic Cooling Using Free Jets and Sprays,” *ASME Journal of Electronic Packaging*, Vol. 117, 1995, pp. 323-332.

- Horacek, B., Kim, J., and Kiger, K. T., "Effects of Noncondensable Gas and Subcooling on the Spray Cooling of an Isothermal Surface," *Proc. ASME IMECE*, Paper No. IMECE-2003-41680, 2003.
- Horacek, B., Kim, J., and Kiger, K. T., "Gas Effects on Spray Cooling of an Isothermal Surface: Visualization and Time and Space Resolved Heat Transfer Measurements," *Proc. 42nd AIAA Aerospace Sciences Meeting and Exhibit*, Paper No. AIAA-2004-1345, 2004.
- Incropera, F. and D. DeWitt, Fundamentals of Heat and Mass Transfer, 5th ed. New York: John Wiley & Sons, Inc., 2002, pp. 596-601.
- Kim, J., "Spray Cooling Heat Transfer: The State of the Art," *International Journal of Heat and Fluid Flow*, Vol. 28, No. 4, 2007, pp. 753-767.
- Lin, L., and Ponnappan, R., "Heat Transfer Characteristics of Spray Cooling in a Closed Loop," *Intl. J. Heat and Mass Transfer*, Vol. 46, 2003, pp. 3737-3746.
- McMurry, J. and R. Fay, Chemistry, 3rd ed. Upper Saddle River, New Jersey: Prentice-Hall, Inc., 1995, pp. 444-446.
- Michalak, T. E., Yerkes, K. L., Puterbaugh, R., Thomas, S. K., and McQuillen, J., "Cooling Performance of a Partially-Confined FC-72 Spray: The Effect of Variable Gravity," *Proc. 45th AIAA Aerospace Sciences Meeting and Exhibit*, Paper No. AIAA-2007-198, 2007.
- Milke, J. A., Tinker, S. C., and diMarzo, M., "Effect of Dissolved Gases on Spray Evaporative Cooling with Water," *Fire Technology*, 2nd Quarter, Vol. 33, No. 2, 1997, pp. 99-113.
- Mudawar, I., and Maddox, D. E., "Critical Heat Flux in Subcooled Flow Boiling of Fluorocarbon Liquid on a Simulated Electronic Chip in a Vertical Rectangular Channel," *Int. J. Heat and Mass Transfer*, Vol. 32, No. 2, 1989, pp. 379-394.
- Mudawar, I., "Assessment of High-Heat-Flux Thermal Management Schemes," *IEEE Transactions on Components and Packaging Technologies*, Vol. 24, No. 2, 2001, pp. 122-141.
- Oliphant, K., Webb, B.W., and McQuay, M.Q., "An Experimental Comparison of Liquid Jet Array and Spray Impingement Cooling in the Non-Boiling Regime," *Experimental Thermal and Fluid Science*, Vol. 18, No. 1, 1998, pp. 1-10.
- Rainey, K. N., You, S. M., and Lee, S., "Effect of Pressure, Subcooling, and Dissolved Gas on Pool Boiling Heat Transfer from Microporous Surfaces in FC-72," *ASME J. Heat Transfer*, Vol. 125, 2003, pp. 75-83.

- Rybicki, J. R., and Mudawar, I., "Single-Phase and Two-Phase Cooling Characteristics of Upward-Facing and Downward-Facing Sprays," *Int. J. Heat and Mass Transfer*, Vol. 49, No. 1-2, 2006, pp. 5-16.
- Smith, F. L., Harvey, A. H., "Avoid Common Pitfalls When Using Henry's law," *Chemical Engineering Progress*, Vol. 103, No. 9, 2007, pp. 33-40.
- Xie, H., and Zhiwei, Z., "A Model for Droplet Evaporation Near Leidenfrost Point," *Intl. J. Heat and Mass Transfer*, Vol. 50, 2007, pp. 5328-5333.
- Yerkes, K. L. and Beam, J. E., "Arterial Heat Pipe Performance in a Transient Heat Flux and Body Force Environment," *SAE Aerotech Conference*, Paper No. SAE 921944, 1992.
- Yerkes, K. L., Michalak, T. E., Baysinger, K. M., Puterbaugh, R. L., Thomas, S. K., and McQuillen, J., "Variable-Gravity Effects on a Single-Phase Partially Confined Spray Cooling System," *Journal of Thermophysics and Heat Transfer*, Vol. 20, No. 3, 2006, pp. 361-370.
- Yang Cheng., Tay, A. A. O., and Xue Hong, "An Experimental Study of Liquid Jet Impingement Cooling of Electronic Components With and Without Boiling," *Advances in Electronic Materials and Packaging*, 2001, pp. 369-375.
- Yang, Z., Peng, X. F., and Ye, P., "Numerical and Experimental Investigation of Two Phase Flow During Boiling in a Coiled Tube," *International Journal of Heat and Mass Transfer*, Vol. 51, 2008, pp. 1003-1016.
- Zhang, H. Y., Pinjala, D., and Wong, T.N., "Experimental Characterization of Flow Boiling Heat Dissipation in a Microchannel Heat Sink with Different Orientations," *Proc. 7th IEEE Electronic Packaging Technology Conference*, Vol. 2, 2005, pp. 670-676.